Elastoplastic and limit analysis of 3D steel assemblies using second-order cone programming and dual finite-elements

Chadi El Boustani, Jeremy Bleyer, Mathieu Arquier, Mohammed-Khalil Ferradi, Karam Sab

Elastoplastic and limit analysis of 3D steel assemblies using second-order cone programming and dual finite-elements

Chadi El Boustani[a,b], Jeremy Bleyer[a,*], Mathieu Arquier[b], Mohammed-Khalil Ferradi[b], Karam Sab[a]

[a] *Laboratoire Navier, Ecole des Ponts ParisTech, Univ Gustave Eiffel, CNRS, 77455 Marne-la-Vallée, FRANCE*
[b] *Strains, 75012 Paris, FRANCE*

Abstract

We investigate the use of a second-order cone programming (SOCP) framework for computing complex 3D steel assemblies in the context of elastoplasticity and limit analysis. Displacement and stress-based variational formulations are considered and appropriate finite-element discretization strategies are chosen, yielding respectively an upper and lower bound estimate of the exact solution. An efficient interior-point algorithm is used to solve the associated optimization problems. The discrete solution convergence is estimated by comparing both static and kinematic solutions, offering a way to perform local mesh adaptation. The proposed framework is illustrated on the design of a moment-transmitting assembly, its performance is assessed by comparison with classical elastoplastic computations using Abaqus and, finally, T-stub resistance and failure mechanisms when assessing the strength of a column base plate are compared with the Eurocodes design rules.

Keywords: second-order cone programming, interior point method, elastoplasticity, limit analysis, equilibrium finite elements, steel assembly

1. Introduction

The verification of steel assemblies poses formidable challenges to the designer when the steel joint geometry becomes complex. On the one hand, normative design methods involve lots of manual verification and, on the other hand, the use of numerical simulation by civil engineers is often limited to crude elastic computations and elastic limit checks, largely underestimating the steel assembly plastic capacity which is taken into account by the design norms. Resorting to a fully non-linear elastoplastic computation on a large scale 3D model is still extremely rare in today's engineering practices, mostly due to the

*Corresponding author
Email addresses: chadi.el-boustani@enpc.fr (Chadi El Boustani), jeremy.bleyer@enpc.fr (Jeremy Bleyer), mathieu.arquier@strains.fr (Mathieu Arquier), mohammed-khalil.ferradi@strains.fr (Mohammed-Khalil Ferradi), karam.sab@enpc.fr (Karam Sab)

difficulty of running such computations which require both time and expertise and often suffer robustness issues which may be detrimental to the structure safety.

Limit analysis theory [1], or more generally yield design theory [2, 3], has been widely used as the basis of many design methods in civil engineering e.g. slope stability factors and footing bearing capacities [4], strut-and-tie models [5], yield line methods for slabs and metal plates [6–8], etc. With the advent of efficient conic programming solvers using interior-point algorithms and dedicated finite-element solution strategies, limit analysis problems can now be solved numerically at a moderate cost. The robustness of such solvers in the context of estimating a structure ultimate load is a decisive advantage over traditional Newton-Raphson-based techniques. Interior-point solvers for conic programming problems has now emerged as the state-of-the-art method for this kind of problems [9–12].

Some contributions also explored the use of this framework for other applications such as granular media [13, 14], contact [15–17], viscoplastic flows [18, 19] or elastoplastic computations [15, 20–22]. The latter case is of interest since limit analysis does not guarantee a unique solution as regards failure mechanisms nor does it enable to compute the structure displacements and total strains. Including elastic strains in a limit analysis model i.e. aiming at computing the ultimate load with an elastoplastic computation circumvents the previously mentioned limitations. Beyond assessing the structure load-bearing capacity, it therefore also enables to check for ultimate strain limits in yielded regions.

In this manuscript, we consider the formulation of elastoplastic problems in a convex optimization framework, sharing therefore close similarities with the formulation of limit analysis problems. This approach was initiated by Maier [23–25] where the incremental problem is reduced to a convex quadratic problem in the case of a piecewise-linear yield criterion. The standard elastic predictor/plastic corrector approach is obtained when the local minimization problem over plastic strain variables is solved exactly (return mapping step) and the stress field balance equations (optimality condition on the displacement field) is expressed as a non-linear function of the total strain. Other approaches may include non-smooth Newton methods [26, 27], general interior-point methods [20], sequential quadratic programming, [28], accelerated proximal gradient methods [29], etc. One can also mention the use of a bi-potential method for non-associative behaviours [30, 31].

Generalizing the results of limit analysis problems and their conic representation depending on the chosen plasticity yield criterion [21, 32], the obtained elastoplastic optimization problem can belong to the class of quadratic programming (QP), second-order cone programming (SOCP) or semi-definite programming (SDP) problems. For instance, one obtains QP problems for piecewise-linear yield surfaces, SOCP for 2D or 3D von Mises yield surface [15, 22] or SDP for 3D Mohr-Coulomb yield criterion [11]. Solvers based on the interior-point method (IPM) [33–36] have now emerged as the state-of-the-art technique for solving QP, SOCP or SDP problems. When applied to an elastoplastic computation, this technique exhibits a fundamental difference with classical elastic predictor/plastic corrector schemes coupled with a Newton-Raphson procedure. Indeed, contrary to the latter which alternates between satisfying global equilibrium and verifying the plasticity conditions, the IPM method will produce a sequence of iterates which satisfy none of the two conditions except at convergence. This specific feature is at the origin of the good robustness of the

method in this context [28].

When discretizing in time the rate equations of plasticity, it is assumed that the evolution is monotonous over time during the time increment (no elastic unloading occurs) so that the obtained formulation is that of *holonomic* or *finite-deformation* plasticity. In many cases of interest, one looks for an ultimate state solution under proportional loading for which such formulations are appropriate. Otherwise, one needs to discretize the entire load path into smaller increments over which holonomic plasticity formulations can be adopted. In the former case, we advocate for the use of a single large load increment for computing the structure elastoplastic ultimate state if one is not interested in details by the elastic phase. The robustness of the IPM enables to solve this large load step efficiently, contrary to more classical procedures.

The purpose of the present manuscript is to provide a general framework for computing efficiently the ultimate state of complex steel assemblies including plasticity. Following on the ideas of [17], we will resort to a dual finite-element discretization involving kinematic displacement-based elements as well as static equilibrium-based elements providing, respectively, an upper and lower bounds estimate to the exact solution and, in particular, to the exact structure ultimate load. Both computations can be also be used to compute a constitutive error indicator which can be used in a remeshing algorithm.

The present paper will therefore include:

- a presentation of the incremental variational formulations of elastoplastic boundary value problems and their extension to limit analysis/yield design (sections 2 and 3);
- the finite-element discretizations used in both approaches along with some comments on the interior-point solution procedure (section 4);
- illustrative examples aiming at:
  - showing how the method can be used to analyse a typical steel assembly and be a valuable tool for the design procedure (section 5.1);
  - assessing its performance and accuracy with respect to classical elastoplastic solution strategies (section 5.2);
  - validate the method against Eurocodes design norms (section 5.3) .

2. Variational formulation for elastoplasticity

In the following, $\boldsymbol{u}$ will denote the displacement field on the solid domain Ω, $\boldsymbol{\varepsilon}_{(\boldsymbol{u})} = \boldsymbol{\nabla}^S \boldsymbol{u}$ the linearized strain tensor, $\boldsymbol{\sigma}$ for the Cauchy stress tensor and $\boldsymbol{\varepsilon}^p$ for plastic strains. Imposed displacements and surface tractions will be respectively denoted by $\boldsymbol{u}_d$ (prescribed on $\Gamma_{\boldsymbol{u}}$) and $\boldsymbol{t}_d$ (prescribed on $\Gamma_{\boldsymbol{t}}$). Body forces will be noted $\boldsymbol{b}$ and we will restrict here to quasi-static loadings. The normal vector $\boldsymbol{n}$ pointing outwards will be used to orient free faces and surfaces. Finally, $\Sigma_{\boldsymbol{\sigma}}$ will denote an internal surface of potential stress discontinuities (see figure 1).

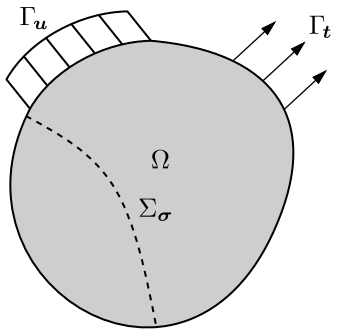

Figure 1: Reference model

We will consider an elasto-plastic von Mises material with linear isotropic hardening, although more general hardening models could well be considered. Its free energy density is given by:

$$\psi(\boldsymbol{\varepsilon}, \boldsymbol{\varepsilon}^p, p) = \frac{1}{2}(\boldsymbol{\varepsilon} - \boldsymbol{\varepsilon}^p) : \mathbb{C} : (\boldsymbol{\varepsilon} - \boldsymbol{\varepsilon}^p) + \frac{1}{2} E_h p^2 \tag{2.1}$$

where $\mathbb{C}$ is the elasticity stiffness tensor, E_h the hardening modulus and $p(t) = \int_0^t \sqrt{\frac{2}{3}} \|\dot{\boldsymbol{\varepsilon}}^p\| dt$ the accumulated plastic strain where $\|\boldsymbol{a}\| = \sqrt{a_{ij} a_{ij}}$. The plastic dissipation potential is given by:

$$\phi(\dot{\boldsymbol{\varepsilon}}^p) = \begin{cases} \sqrt{\frac{2}{3}} \sigma_0 \|\dot{\boldsymbol{\varepsilon}}^p\| & \text{if } \operatorname{tr}(\dot{\boldsymbol{\varepsilon}}^p) = 0 \\ +\infty & \text{otherwise} \end{cases} \tag{2.2}$$

corresponding to the von Mises plastic yield criterion:

$$f(\boldsymbol{\sigma}, p) = \sqrt{\frac{3}{2}} \|\operatorname{dev}(\boldsymbol{\sigma})\| - (\sigma_0 + E_h.p) \tag{2.3}$$

We now focus on an incremental formulation between times $[t_n, t_{n+1}]$ among the total time interval $[0, T]$. Knowing all mechanical fields at time t_n, the unknown fields at time t_{n+1} can be obtained from the solution of the following incremental variational formulation [37, 38]:

$$\underset{\boldsymbol{u}, \boldsymbol{\varepsilon}^p, p}{\arg\min} \int_\Omega \int_{t_n}^{t_{n+1}} (\dot{\psi}(\boldsymbol{\varepsilon}, \boldsymbol{\varepsilon}^p, p) + \phi(\dot{\boldsymbol{\varepsilon}}^p)) dt d\Omega - \int_{t_n}^{t_{n+1}} P_{ext}(\dot{\boldsymbol{u}}) dt \tag{2.4}$$

where P_{ext} is the power of external loads.

An approximate solution to (2.4) can be obtained by restricting the above variational formulation to evolutions on $[t_n, t_{n+1}]$ in which plastic strain rates are assumed to be constant over the time interval:

$$\dot{\boldsymbol{\varepsilon}}^p(t) = \frac{\boldsymbol{\varepsilon}^p_{n+1} - \boldsymbol{\varepsilon}^p_n}{t_{n+1} - t_n} \tag{2.5}$$

where we wrote explicitly the time dependence but not the spatial one, $\dot{\boldsymbol{\varepsilon}}^p, \boldsymbol{\varepsilon}^p_{n+1}, \boldsymbol{\varepsilon}^p_n$ all being tensorial fields.

More generally, we get the same final result if restricting to the more general case of plastic strain rates following radial evolutions over $[t_n, t_{n+1}]$ i.e.:

$$\dot{\boldsymbol{\varepsilon}}^p(t) = \dot{\lambda}(t)\frac{\boldsymbol{\varepsilon}^p_{n+1} - \boldsymbol{\varepsilon}^p_n}{\lambda(t_{n+1}) - \lambda(t_n)} \tag{2.6}$$

so that $\int_{t_n}^{t_{n+1}} \dot{\boldsymbol{\varepsilon}}^p(t)dt = \boldsymbol{\varepsilon}^p_{n+1} - \boldsymbol{\varepsilon}^p_n$. In the above, $\lambda(t)$ is any increasing scalar field i.e. with $\dot{\lambda}(t) \geq 0$ and obviously encompasses (2.6) for $\lambda(t) = t$. With these assumptions and owing to the fact that ϕ is positively-homogeneous, we get that:

$$\int_{t_n}^{t_{n+1}} \phi(\dot{\boldsymbol{\varepsilon}}^p)dt = \int_{t_n}^{t_{n+1}} \frac{\dot{\lambda}(t)}{\lambda(t_{n+1}) - \lambda(t_n)}\phi(\boldsymbol{\varepsilon}^p_{n+1} - \boldsymbol{\varepsilon}^p_n)dt = \phi(\boldsymbol{\varepsilon}^p_{n+1} - \boldsymbol{\varepsilon}^p_n) \tag{2.7}$$

As a result, an approximate solution to (2.4) is given by:

$$\begin{aligned}(\boldsymbol{u}_{n+1}, \boldsymbol{\varepsilon}^p_{n+1}, p_{n+1}) = \underset{\boldsymbol{u},\boldsymbol{\varepsilon}^p,p}{\arg\min} \quad & \int_\Omega \left(\psi(\boldsymbol{\varepsilon}, \boldsymbol{\varepsilon}^p, p) - \psi(\boldsymbol{\varepsilon}_n, \boldsymbol{\varepsilon}^p_n, p_n) + \phi\left(\boldsymbol{\varepsilon}^p - \boldsymbol{\varepsilon}^p_n\right)\right) d\Omega \\ & -P_{ext}(\boldsymbol{u} - \boldsymbol{u}_n)\end{aligned} \tag{2.8}$$

The optimality conditions of this incremental problem yield the classical relations of holonomic plasticity. The solution also coincides with that obtained from classical return mapping procedure using a backward Euler discretization in time. Let us recall again that the obtained solution is only approximate but usually of good quality, especially for proportional loadings.

Denoting by $\Delta\boldsymbol{\varepsilon} = \boldsymbol{\varepsilon}_{n+1} - \boldsymbol{\varepsilon}_n$ the strain increment and injecting (2.1) and (2.2), the minimization problem becomes:

$$\begin{aligned}\min_{\Delta\boldsymbol{u},\Delta\boldsymbol{\varepsilon}^p,\Delta p} \quad & \int_\Omega \Big(\frac{1}{2}(\Delta\boldsymbol{\varepsilon} - \Delta\boldsymbol{\varepsilon}^p) : \mathbb{C} : (\Delta\boldsymbol{\varepsilon} - \Delta\boldsymbol{\varepsilon}^p) + \boldsymbol{\sigma}_n : (\Delta\boldsymbol{\varepsilon} - \Delta\boldsymbol{\varepsilon}^p) \\ & + \frac{1}{2}E_h\Delta p^2 + E_h p_n \Delta p + \sqrt{\frac{2}{3}}\sigma_0\|\Delta\boldsymbol{\varepsilon}^p\|\Big) d\Omega - P_{ext}(\Delta\boldsymbol{u}) \\ \text{s.t.} \quad & \mathrm{tr}(\Delta\boldsymbol{\varepsilon}^p) = 0\end{aligned} \tag{2.9}$$

Since $\dot{p} = \sqrt{\frac{2}{3}}\|\dot{\boldsymbol{\varepsilon}}^p\|$, we also have $\Delta p = \sqrt{\frac{2}{3}}\|\Delta\boldsymbol{\varepsilon}^p\|$ therefore

$$E_h p_n \Delta p + \sqrt{\frac{2}{3}}\sigma_0\|\Delta\boldsymbol{\varepsilon}^p\| = \sqrt{\frac{2}{3}}\sigma_{Y,n}\|\Delta\boldsymbol{\varepsilon}^p\|$$

and

$$\frac{1}{2}E_h(\Delta p)^2 = \frac{1}{3}E_h\|\Delta\boldsymbol{\varepsilon}^p\|^2$$

with $\sigma_{Y,n} = \sigma_0 + E_h.p_n$.

Writing explicitly the link between the displacement and total strain increments and the Dirichlet boundary conditions, we have:

$$\min_{\Delta \boldsymbol{u},\, \Delta \boldsymbol{\varepsilon}^p} \quad \int_\Omega \left[\frac{1}{2}(\Delta\boldsymbol{\varepsilon} - \Delta\boldsymbol{\varepsilon}^p) : \mathbb{C} : (\Delta\boldsymbol{\varepsilon} - \Delta\boldsymbol{\varepsilon}^p) + (\boldsymbol{\varepsilon}_n - \boldsymbol{\varepsilon}_n^p) : \mathbb{C} : (\Delta\boldsymbol{\varepsilon} - \Delta\boldsymbol{\varepsilon}^p) \right.$$
$$\left. + \frac{1}{3} E_h \|\Delta\boldsymbol{\varepsilon}^p\|^2 + \sqrt{\frac{2}{3}} \sigma_{Y,n} \|\Delta\boldsymbol{\varepsilon}^p\| \right] d\Omega - P_{ext}(\Delta\boldsymbol{u}) \tag{2.10a}$$

$$\text{subject to} \quad \Delta\boldsymbol{\varepsilon} = \boldsymbol{\nabla}^S(\Delta\boldsymbol{u}) \qquad \text{in } \Omega \tag{2.10b}$$

$$\Delta\boldsymbol{u} + \boldsymbol{u}_n = \boldsymbol{u}_{d,n+1} \qquad \text{on } \Gamma_{\boldsymbol{u}} \tag{2.10c}$$

$$\mathrm{tr}(\Delta\boldsymbol{\varepsilon}^p) = 0 \qquad \text{in } \Omega \tag{2.10d}$$

This optimization problem fits into the conic programming framework for which interior point methods are well suited. Indeed, one can for instance introduce an auxiliary scalar variable $\Delta\gamma$ such that $\Delta\gamma \geq \|\Delta\boldsymbol{\varepsilon}^p\|$. The previous problem can then be equivalently reformulated as:

$$\min_{\Delta \boldsymbol{u},\Delta\boldsymbol{\varepsilon}^p,\Delta\gamma} \quad \int_\Omega \left[\frac{1}{2}(\Delta\boldsymbol{\varepsilon} - \Delta\boldsymbol{\varepsilon}^p) : \mathbb{C} : (\Delta\boldsymbol{\varepsilon} - \Delta\boldsymbol{\varepsilon}^p) + (\boldsymbol{\varepsilon}_n - \boldsymbol{\varepsilon}_n^p) : \mathbb{C} : (\Delta\boldsymbol{\varepsilon} - \Delta\boldsymbol{\varepsilon}^p) \right.$$
$$\left. + \frac{1}{3} E_h (\Delta\gamma^2) + \sqrt{\frac{2}{3}} \sigma_{Y,n} \Delta\gamma \right] d\Omega - P_{ext}(\Delta\boldsymbol{u}) \tag{2.11a}$$

$$\text{subject to} \quad \Delta\boldsymbol{\varepsilon} = \boldsymbol{\nabla}^S(\Delta\boldsymbol{u}) \qquad \text{in } \Omega \tag{2.11b}$$

$$\Delta\boldsymbol{u} + \boldsymbol{u}_n = \boldsymbol{u}_{d,n+1} \qquad \text{on } \Gamma_{\boldsymbol{u}} \tag{2.11c}$$

$$\mathrm{tr}(\Delta\boldsymbol{\varepsilon}^p) = 0 \qquad \text{in } \Omega \tag{2.11d}$$

$$\|\Delta\boldsymbol{\varepsilon}^p\| \leq \Delta\gamma \qquad \text{in } \Omega \tag{2.11e}$$

The traceless constraint on $\Delta\boldsymbol{\varepsilon}^p$ can be removed by introducing directly the deviatoric operator dev() in the elastic constitutive relation as shown in [22] :

$$\boldsymbol{\sigma}_{n+1} = \boldsymbol{\sigma}_n + \mathbb{C} : (\Delta\boldsymbol{\varepsilon} - \mathrm{dev}(\Delta\boldsymbol{\varepsilon}^p)) \tag{2.12}$$

The previous optimisation problem is then changed to:

$$J_{\text{kin}} = \min_{\Delta\boldsymbol{u},\,\Delta\boldsymbol{\varepsilon}^p,\,\Delta\gamma} \int_\Omega \left[\frac{1}{2}(\Delta\boldsymbol{\varepsilon} - \text{dev}(\Delta\boldsymbol{\varepsilon}^p)) : \mathbb{C} : (\Delta\boldsymbol{\varepsilon} - \text{dev}(\Delta\boldsymbol{\varepsilon}^p)) + \boldsymbol{\sigma}_n : (\Delta\boldsymbol{\varepsilon} - \text{dev}(\Delta\boldsymbol{\varepsilon}^p)) + \frac{1}{3}E_h(\Delta\gamma)^2 + \sqrt{\frac{2}{3}}\sigma_{Y,n}\Delta\gamma\right] d\Omega - P_{ext}(\Delta\boldsymbol{u}) \tag{2.13a}$$

$$\text{subject to} \quad \Delta\boldsymbol{\varepsilon} = \boldsymbol{\nabla}^S(\Delta\boldsymbol{u}) \qquad \text{in } \Omega \tag{2.13b}$$

$$\Delta\boldsymbol{u} + \boldsymbol{u}_n = \boldsymbol{u}_{d,n+1} \qquad \text{on } \Gamma_{\boldsymbol{u}} \tag{2.13c}$$

$$\|\Delta\boldsymbol{\varepsilon}^p\| \leq \Delta\gamma \qquad \text{in } \Omega \tag{2.13d}$$

Similarly, the dual minimisation problem acting on statically admissible stress fields $\boldsymbol{\sigma} \in SA(\Omega)$ is expressed as follows [15, eq. (11.61)]

$$J_{\text{stat}} = \min_{\boldsymbol{\sigma}_{n+1},\,\sigma_{Y,n+1}} \int_\Omega \left[\frac{1}{2}(\boldsymbol{\sigma}_{n+1} - \boldsymbol{\sigma}_n) : \mathbb{C}^{-1} : (\boldsymbol{\sigma}_{n+1} - \boldsymbol{\sigma}_n) + \frac{1}{2E_h}(\sigma_{Y,n+1} - \sigma_{Y,n})^2\right] d\Omega - \int_{\Gamma_{\boldsymbol{u}}} (\boldsymbol{\sigma}_{n+1}.\boldsymbol{n}).(\boldsymbol{u}_{d,n+1} - \boldsymbol{u}_{d,n}) d\Gamma \tag{2.14a}$$

$$\text{subject to} \quad \text{Div}(\boldsymbol{\sigma}_{n+1}) + \boldsymbol{b}_{n+1} = 0 \qquad \text{in } \Omega \tag{2.14b}$$

$$[\![\boldsymbol{\sigma}_{n+1}]\!].\boldsymbol{n} = 0 \qquad \text{on } \Sigma_\sigma \tag{2.14c}$$

$$\boldsymbol{\sigma}_{n+1}.\boldsymbol{n} = \boldsymbol{t}_{d,n+1} \qquad \text{on } \Gamma_{\boldsymbol{t}} \tag{2.14d}$$

$$\sqrt{\frac{3}{2}}\|\text{dev}(\boldsymbol{\sigma}_{n+1})\| \leq \sigma_{Y,n+1} \qquad \text{in } \Omega \tag{2.14e}$$

As a result, both objective functions are opposite $-J_{\text{stat}} = J_{\text{kin}}$ for the true elastoplastic solution. When restricting both minimum problems to finite-dimensional subspace obtained from a finite-element discretization for instance, both objective functions will differ and under careful choice on how discretization is performed, the kinematic approach will yield an upper bound to the true solution, whereas the static approach will yield a lower bound: $-J_{\text{stat},h} \leq -J_{\text{stat}} = J_{\text{kin}} \leq J_{\text{kin},h}$. It must be kept in mind that the discrete optimization problems associated with $J_{\text{stat},h}$ and $J_{\text{kin},h}$ are not dual to each other in the convex optimization sense since they are associated with different discretization strategies. They however offer a bracketing of the true solution since the accuracy of the discretized

solution can be compared by computing $J_{\text{kin},h} + J_{\text{stat},h}$ (see [17]). We later refer to this quantity as the primal-dual gap i.e. the discretization gap between the primal (kinematic) discretization and the dual (static) discretization.

The increment solution of an elasto-plastic problem can then be obtained from the resolution of a convex optimization problem in terms of the displacement and plastic strain increments for the kinematic formulation or in terms of the new stress and yield limit at time t_{n+1} for the dual static formulation. With a von Mises material, both problems fall into the class of second-order cone programming problems for which interior-point algorithms are well suited. Let us mention that we can also add unilateral or associated frictional contact conditions to both formulations following the lines of [17] without changing the second-order cone nature of the problem.

3. Modification for yield analysis optimisation problems

Upper and lower bound yield analysis theorems enable to estimate the load bearing capacity of a structure subject to a given strength criterion. The numerical resolution of finite-element discretized yield analysis can also be efficiently achieved using interior point methods for conic programming [9, 10, 39, 40]. One can easily obtain these two lower and upper bound problems from formulations (2.13a) and (2.14a) by considering a rigid perfectly plastic material i.e. $\mathbb{C} \to \infty$ hence $\boldsymbol{\varepsilon} = \boldsymbol{\varepsilon}^p$ and $E_h = 0$. Besides, in order to obtain the maximum load factor, we consider that the loading consist of a fixed part (e.g. the body forces $\boldsymbol{b}$) and a reference loading scaled by a load multiplier α (e.g. for the surface tractions $\alpha \boldsymbol{t}$) which we want to maximize. In this case, the work of external loads take the following form:

$$\alpha P_{ext}(\boldsymbol{u}) + P_{ext,0}(\boldsymbol{u}) = \alpha \int_{\Gamma_t} \boldsymbol{t} \cdot \boldsymbol{u} d\Gamma + \int_{\Omega} \boldsymbol{b} \cdot \boldsymbol{u} d\Omega$$

Considering only homogeneous Dirichlet boundary conditions for simplicity, problems (2.13a) and (2.14a) respectively become:

$$\begin{aligned} \alpha_{upper} = \quad & \min_{\boldsymbol{u},\, \boldsymbol{\varepsilon}^p,\, \gamma} \quad \int_{\Omega} \sqrt{\frac{2}{3}} \sigma_0 \gamma d\Omega - P_{ext,0}(\boldsymbol{u}) \\ & \text{subject to} \quad \boldsymbol{\varepsilon}_p = \boldsymbol{\nabla}^S \boldsymbol{u} \qquad \text{in } \Omega \\ & \qquad\qquad\; \boldsymbol{u} = 0 \qquad\qquad\; \text{on } \Gamma_{\boldsymbol{u}} \\ & \qquad\qquad\; P_{ext}(\boldsymbol{u}) = 1 \\ & \qquad\qquad\; \text{tr}(\boldsymbol{\varepsilon}^p) = 0 \qquad\qquad \text{in } \Omega \\ & \qquad\qquad\; \|\boldsymbol{\varepsilon}^p\| \leq \Delta\gamma \qquad\qquad \text{in } \Omega \end{aligned} \tag{3.1}$$

$$
\begin{aligned}
\alpha_{lower} = \quad & \underset{\alpha,\,\boldsymbol{\sigma}}{\text{maximize}} \quad \alpha \\
& \text{subject to} \quad \operatorname{Div}(\boldsymbol{\sigma}) + \boldsymbol{b} = 0 \qquad \text{in } \Omega \\
& \qquad\qquad [\![\boldsymbol{\sigma}]\!].\boldsymbol{n} = 0 \qquad \text{on } \Sigma_\sigma \\
& \qquad\qquad \boldsymbol{\sigma}.\boldsymbol{n} = \alpha \boldsymbol{t}_d \qquad \text{on } \Gamma_{\boldsymbol{t}} \\
& \qquad\qquad \sqrt{\frac{3}{2}} \|\operatorname{dev}(\boldsymbol{\sigma})\| \leq \sigma_0 \qquad \text{in } \Omega
\end{aligned}
\tag{3.2}
$$

in which the optimal objective values respectively produce an upper and lower bound estimate of the true collapse load multiplier α^+: $\alpha_{\text{lower}} \leq \alpha^+ \leq \alpha_{\text{upper}}$.

4. Finite-element discretizations and solution procedure

In this section, we briefly describe the different finite-element discretizations that we can use for solving problem (2.13a) or (2.14a).

4.1. Kinematic approach

4.1.1. Continuous discretization

Standard continuous displacement-type discretization with 10-node quadratic tetrahedra are used to solve the upper bound problem (2.13a) . The element degrees of freedom (DoF) are the following:

- $3 \times 10 = 30$ nodal displacement increments $\Delta \boldsymbol{u}$;
- $6 \times n_G$ plastic strain increments $\Delta \boldsymbol{\varepsilon}_p$ at each integration point;
- n_G scalar auxiliary variables $\Delta\gamma$ at each integration point;

where n_G is the number of quadrature points per tetrahedron for numerical integration (minimum 4). Let $\boldsymbol{x}$ be the aggregation of of a single tetrahedron DoF i.e. for $n_G = 4$:

$$
\boldsymbol{x} = (30\,\Delta\boldsymbol{u}, 24\,\Delta\boldsymbol{\varepsilon}_p, 4\Delta\gamma)
$$

Let $\boldsymbol{B}$ be the strain-displacement matrix operator and $\boldsymbol{D}$ the deviatoric matrix operator. The elementary stiffness matrix for each tetrahedron can then be calculated taking into account the traceless condition for $\Delta\boldsymbol{\varepsilon}^p$ as follows:

$$
\boldsymbol{K}_e = \left[\begin{array}{c|c|c}
\boldsymbol{B}^T \mathbb{C} \boldsymbol{B} & -\boldsymbol{B}^T \mathbb{C} \boldsymbol{D} & 0 \\
\hline
-\boldsymbol{D}^T \mathbb{C} \boldsymbol{B} & \boldsymbol{D}^T \mathbb{C} \boldsymbol{D} & 0 \\
\hline
0 & 0 & \dfrac{2}{3} E_h
\end{array}\right]
\tag{4.1}
$$

Problem (2.13a) can then be expressed after assembling the global stiffness matrix $\hat{\boldsymbol{K}}$, the nodal plastic dissipation vector $\hat{\boldsymbol{d}}$ and the nodal force vector $\hat{\boldsymbol{f}}$ as a conic minimization problem using the SOCP formalism as follows:

$$\begin{aligned} \min_{\hat{\boldsymbol{x}}} \quad & \frac{1}{2}\Delta\hat{\boldsymbol{x}}^T\hat{\boldsymbol{K}}\Delta\hat{\boldsymbol{x}}^T + \hat{\boldsymbol{K}}\hat{\boldsymbol{x}}_n\Delta\hat{\boldsymbol{x}}^T + \hat{\boldsymbol{d}}^T\Delta\hat{\boldsymbol{x}}^T - \hat{\boldsymbol{f}}_{n+1}^T\Delta\hat{\boldsymbol{x}}^T \\ \text{s.t.} \quad & \Delta\hat{\boldsymbol{u}} + \hat{\boldsymbol{u}}_n = \hat{\boldsymbol{u}}_{d,n+1} \qquad \text{on } \Gamma_{\boldsymbol{u}} \\ & \|\Delta\boldsymbol{\varepsilon}^p\| \leq \Delta\gamma \qquad \text{at each integration point} \end{aligned} \tag{4.2}$$

in which the primal optimization variables are $\hat{\boldsymbol{x}} = (\Delta\hat{\boldsymbol{u}}, \Delta\hat{\boldsymbol{\varepsilon}}_p, \Delta\gamma)$. As mentioned previously, contact constraints can be added and enforced at all 6 nodes of each face following [17]. After introducing a proper change of variable, the contact conditions can be easily transformed into a standard second-order cone constraint using a Lorentz cone. Let us finally mention that, for the above formulation to yield a true upper bound of the exact response, quadrature points (i.e. the location at which plastic flow rule will be enforced) have to be located at the tetrahedra vertices (see [10]). However, in practice, choosing standard Gauss points yields a very close response.

4.1.2. Discontinuous mesh

The plastic condition is known for inducing volumetric locking problems, even for quadratic tetrahedra. One possible remedy consists in considering a fully discontinuous displacement interpolation and accounting for the displacement jump contribution to the plastic dissipation potential:

$$\phi(\llbracket\Delta\boldsymbol{u}\rrbracket) = \begin{cases} \sqrt{\frac{1}{3}}\sigma_0\|\llbracket\Delta\boldsymbol{u}.\boldsymbol{t}\rrbracket\| & \text{if } \llbracket\Delta\boldsymbol{u}.\boldsymbol{n}\rrbracket = 0 \\ +\infty & \text{otherwise} \end{cases} \tag{4.3}$$

Note that only tangential discontinuities are allowed and that the full displacement jump contributes to the plastic potential, meaning that no discontinuity will occur during the purely elastic phase. Similarly to the bulk plastic dissipation, an auxiliary scalar variable $\Delta\zeta$ must be introduced such that $\Delta\zeta \geq \|\llbracket\Delta\boldsymbol{u}.\boldsymbol{t}\rrbracket\|$ in order to fit into the conic formalism.

The introduction of discontinuities prevents volumetric locking and also improves the discretization accuracy as will be shown in section 5. However, it introduces additional degrees of freedom since each tetrahedron displacements are now independent. This implies higher computational times which can reach 4 to 10 times those of the continuous kinematic approach.

4.1.3. Hybrid formulation

One other remedy for mitigating locking effects is to resort to a so-called mixed, or hybrid, discretization in which the traceless condition (2.11d) is enforced only on average on each element, instead of being enforced at each quadrature point as it should be. Note that, in this case, the bounding character of the kinematic approach is inevitably lost.

4.2. Static approach

For the static approach, we use improved equilibrium elements based on the formulations given in [41–43] but accounting for some changes to fit into the convex optimization framework. To simplify notations isotropic hardening is not considered and the time increments are dropped so that problem (2.14a) becomes:

$$\min_{\boldsymbol{\sigma}} \quad \int_{\Omega} \frac{1}{2}\boldsymbol{\sigma} : \mathbb{C}^{-1} : \boldsymbol{\sigma} d\Omega - \int_{\Gamma_{\boldsymbol{u}}} (\boldsymbol{\sigma}.\boldsymbol{n}).\boldsymbol{u}_d d\Gamma \tag{4.4a}$$

$$\text{s.t.} \quad \operatorname{Div}(\boldsymbol{\sigma}) + \boldsymbol{b} = 0 \qquad \text{in } \Omega \tag{4.4b}$$

$$[\![\boldsymbol{\sigma}]\!].\boldsymbol{n} = 0 \qquad \text{on } \Sigma_{\boldsymbol{\sigma}} \tag{4.4c}$$

$$\boldsymbol{\sigma}.\boldsymbol{n} = \boldsymbol{t}_d \qquad \text{on } \Gamma_{\boldsymbol{t}} \tag{4.4d}$$

$$\sqrt{\frac{3}{2}} \| \operatorname{dev}(\boldsymbol{\sigma}) \| \leq \sigma_0 \quad \text{in } \Omega \tag{4.4e}$$

When introducing Lagrange multipliers associated with the linear constraint (4.4c), these can be interpreted as displacements of each internal facet of the mesh. Similarly, Lagrange multipliers associated with constraint (4.4d) can be interpreted as displacement of faces lying on the boundary $\Gamma_{\boldsymbol{t}}$. Denoting by $\boldsymbol{u}$ both internal and external face displacements and prescribing explicitly $\boldsymbol{u} = \boldsymbol{u}_d$ on $\Gamma_{\boldsymbol{u}}$, the previous minimisation problem can be rewritten as follows:

$$\min_{\boldsymbol{\sigma}, \boldsymbol{u}} \quad \int_{\Omega} \frac{1}{2}\boldsymbol{\sigma} : \mathbb{C}^{-1} : \boldsymbol{\sigma} d\Omega - \int_{\Sigma_{\boldsymbol{\sigma}}} [\![\boldsymbol{\sigma}]\!].\boldsymbol{n}.\boldsymbol{u} d\Gamma - \int_{\Gamma_{\boldsymbol{t}}} \boldsymbol{t}_d.\boldsymbol{u} d\Gamma \tag{4.5a}$$

$$\text{s.t.} \quad \operatorname{Div}(\boldsymbol{\sigma}) + \boldsymbol{b} = 0 \qquad \text{in } \Omega \tag{4.5b}$$

$$\boldsymbol{u} = \boldsymbol{u}_d \qquad \text{on } \Gamma_{\boldsymbol{u}} \tag{4.5c}$$

$$\sqrt{\frac{3}{2}} \| \operatorname{dev}(\boldsymbol{\sigma}) \| \leq \sigma_0 \quad \text{in } \Omega \tag{4.5d}$$

Next, appropriate interpolations are chosen for $\boldsymbol{\sigma}$ and $\boldsymbol{u}$. To do so, the stress distribution inside an element is chosen in order to satisfy local equilibrium equations with body forces [41–43] such as:

$$\boldsymbol{\sigma}(\boldsymbol{x}) = \boldsymbol{S}(\boldsymbol{x})\boldsymbol{q} + \boldsymbol{\sigma}_{\boldsymbol{b}}(\boldsymbol{x}) \tag{4.6}$$

where $\boldsymbol{S}$ is a matrix of independent shape functions of degree p, the columns of which $\boldsymbol{S}_k$ all verify $\operatorname{Div}(\boldsymbol{S}_k) = 0$. They can be obtained either from Morera [44] or Maxwell [45] stress potentials. In the following, we consider only linear stress shape functions ($p = 1$) i.e. $\boldsymbol{S}$ is of dimension (6×21). The 21 variables $\boldsymbol{q}$ are the generalized stresses and are not related to any nodes but to the entire finite-element volume. $\boldsymbol{\sigma}_{\boldsymbol{b}}$ is a particular solution for the equilibrium equations with $\boldsymbol{b} \neq 0$ and taken as equal to zero in absence of body forces. For simplicity, we will consider the latter case in the following. The expressions for

the polynomial functions $\boldsymbol{S}$ can be found in [46].

Since, stress fields vary in a linear fashion, equations (4.4c) and (4.4d) can be enforced exactly using a linear interpolation for the face displacement Lagrange multipliers $\boldsymbol{u}$. For face j, the nodal displacement vector is $\boldsymbol{u}^{(j)} = \{u_{x1}, u_{y1}, \ldots, u_{z3}\}$ so that the displacement of an arbitrary point of face j is:

$$\boldsymbol{u}(\boldsymbol{x}) = \boldsymbol{P}_j(\boldsymbol{x})\boldsymbol{u}^{(j)} \tag{4.7}$$

with $\boldsymbol{P}_j$ being linear shape functions. We later denote by $\boldsymbol{u}_e = \{\boldsymbol{u}^{(1)}, \ldots, \boldsymbol{u}^{(4)}\}$ the nodal displacements of all faces and by $\boldsymbol{P}$ the corresponding aggregated shape function matrix.

Using all of these, the elementary matrix for each tetrahedron can be calculated using the first variation of the objective function (4.5a):

$$\delta\boldsymbol{q}^T\boldsymbol{F}\boldsymbol{q} + \delta\boldsymbol{q}^T\boldsymbol{H}^T\boldsymbol{u}_e + \delta\boldsymbol{u}_e^T\boldsymbol{H}\boldsymbol{q} = \delta\boldsymbol{u}_e^T\boldsymbol{f} \qquad \forall(\delta\boldsymbol{q}, \delta\boldsymbol{u}_e) \tag{4.8}$$

where

$$\boldsymbol{F} = \int_{\Omega_e} \boldsymbol{S}^T\mathbb{C}^{-1}\boldsymbol{S}d\Omega \tag{4.9}$$

$$\boldsymbol{H} = \int_{\partial\Omega_e} \boldsymbol{P}^T\boldsymbol{N}\boldsymbol{S}d\Gamma \tag{4.10}$$

$$\boldsymbol{f} = \int_{\partial\Omega_e\cap\Gamma_{\boldsymbol{t}}} \boldsymbol{P}^T\boldsymbol{t}_d d\Gamma \tag{4.11}$$

Equation (4.8) can be rewritten in matrix form :

$$\left[\begin{array}{c|c} \boldsymbol{F} & \boldsymbol{H}^T \\ \hline \boldsymbol{H} & \boldsymbol{0} \end{array}\right] \begin{Bmatrix} \boldsymbol{q} \\ \boldsymbol{u}_e \end{Bmatrix} = \begin{Bmatrix} \boldsymbol{0} \\ \boldsymbol{f} \end{Bmatrix} \tag{4.12}$$

The obtained matrix is singular. As shown in [42], it has 6 zero eigenvalues corresponding to the rigid body movements, and 9 more corresponding to spurious kinematic modes (SKM).

These spurious modes can be eliminated using the *super-element* method, consisting in considering one tetrahedral element as an assembly of four sub-tetrahedra based on each four faces and sharing a common inner vertex lying at the center of the macro-tetrahedron. This combination results in 4 tetrahedrons ($4 \times 21 = 84$ generalized stresses $\hat{\boldsymbol{q}}$), 4 external faces ($4 \times 9 = 36$ external face displacements $\hat{\boldsymbol{u}}_e$) and 6 internal faces ($6 \times 9 = 54$ internal faces displacements $\hat{\boldsymbol{u}}_i$) yielding the corresponding elementary matrix:

$$\left[\begin{array}{c|c|c} \hat{\boldsymbol{F}} & \hat{\boldsymbol{H}}_i^T & \hat{\boldsymbol{H}}_e^T \\ \hline \hat{\boldsymbol{H}}_i & \boldsymbol{0} & \boldsymbol{0} \\ \hline \hat{\boldsymbol{H}}_e & \boldsymbol{0} & \boldsymbol{0} \end{array}\right] \begin{Bmatrix} \hat{\boldsymbol{q}} \\ \hat{\boldsymbol{u}}_i \\ \hat{\boldsymbol{u}}_e \end{Bmatrix} = \begin{Bmatrix} \boldsymbol{0} \\ \boldsymbol{0} \\ \hat{\boldsymbol{f}}_e \end{Bmatrix} \tag{4.13}$$

in which the $\hat{\star}$ symbol is used to denote aggregated matrix/vector over the corresponding degrees of freedom.

The final element matrix is obtained by performing static condensation over the internal degrees of freedom $\hat{\boldsymbol{u}}_i$:

$$\left[\begin{array}{c|c} \hat{\boldsymbol{F}} & \hat{\boldsymbol{H}}_c \\ \hline \hat{\boldsymbol{H}}_e & \boldsymbol{0} \end{array}\right] \left\{\begin{array}{c} \hat{\boldsymbol{q}} \\ \hat{\boldsymbol{u}}_e \end{array}\right\} = \left\{\begin{array}{c} \boldsymbol{0} \\ \hat{\boldsymbol{f}}_e \end{array}\right\} \tag{4.14}$$

where

$$\hat{\boldsymbol{H}}_c = \hat{\boldsymbol{H}}_e^T - \hat{\boldsymbol{H}}_i^T.(\hat{\boldsymbol{H}}_i \hat{\boldsymbol{F}}^{-1} \hat{\boldsymbol{H}}_i^T)^{-1}.(\hat{\boldsymbol{H}}_i \hat{\boldsymbol{F}}^{-1} \hat{\boldsymbol{H}}_e^T) \tag{4.15}$$

Assembling the elementary matrices to a global matrix $\hat{\boldsymbol{A}}$ leads to a minimization problem of the following form:

$$\min_{\hat{\boldsymbol{x}}} \quad \frac{1}{2} \hat{\boldsymbol{x}}^T \hat{\boldsymbol{A}} \hat{\boldsymbol{x}} - \hat{\boldsymbol{f}}^T \hat{\boldsymbol{x}} \tag{4.16a}$$

$$\text{s.t.} \quad \hat{\boldsymbol{u}}_e = \boldsymbol{u}_d \qquad \text{on } \Gamma_{\boldsymbol{u}} \tag{4.16b}$$

$$\sqrt{\frac{3}{2}} \|\boldsymbol{D}\boldsymbol{S}\hat{\boldsymbol{q}}\| \leq \sigma_0 \quad \text{at each vertex} \tag{4.16c}$$

where $\hat{\boldsymbol{x}}$ is the global vector of degrees of freedom containing both $\hat{\boldsymbol{q}}$ and $\hat{\boldsymbol{u}}_e$ for all elements. Note that since the stress field is piecewise linear inside each sub-tetrahedra, it is enough to check the plasticity criterion at each vertex of each sub-tetrahedra to guarantee the lower bound status of the static approach. Similarly, contact constraint can be easily added to the above conic optimization problem. Including back time increments and body forces will only change expressions of right-hand side terms whereas including hardening will have to include the new yield stress as an additional optimization variable with its corresponding quadratic energy term.

4.3. Primal-dual interior point method for SOCP

All final discretized optimization problems (4.2) and (4.16a) (or their variants) share a common structure of the following form:

$$\min_{\boldsymbol{x}} \quad \frac{1}{2} \boldsymbol{x}^T \boldsymbol{K} \boldsymbol{x} - \boldsymbol{f}^T \boldsymbol{x} \tag{4.17a}$$

$$\text{s.t.} \quad \boldsymbol{A}\boldsymbol{x} = \boldsymbol{b} \tag{4.17b}$$

$$\boldsymbol{x} \in \mathcal{K} \tag{4.17c}$$

where $\mathcal{K}$ is a product of cones which can either be the full real line $\mathbb{R}$ (free variable), the positive orthant or Lorentz second-order cones (see [17]). More precisely, the optimization variables can be split in two different groups: $\boldsymbol{x} = (\boldsymbol{x}_g, \boldsymbol{x}_l)$ where $\boldsymbol{x}_g$ denotes global degrees of freedom (coupled by equilibrium equations or the gradient operator) and $\boldsymbol{x}_l$ denotes local degrees of freedom which are uncoupled from one element to another. For instance,

in the kinematic approach (4.2), global degrees of freedom are the displacement increments $\boldsymbol{x}_g = \Delta\hat{\boldsymbol{u}}$ whereas plastic strain increments and auxiliary variables are local degrees of freedom $\boldsymbol{x}_l = (\Delta\hat{\boldsymbol{\varepsilon}}_p, \Delta\gamma)$. Similarly, in the static approach (4.16a), the face displacements are global degrees of freedom $\boldsymbol{x}_g = \hat{\boldsymbol{u}}_e$ whereas generalized stresses are local degrees of freedom $\boldsymbol{x}_l = \hat{\boldsymbol{q}}$. For both cases, it turns out that conic constraints act only on local degrees of freedom at each quadrature point. Besides, linear constraints involve only global degrees of freedom so that the previous problem has in fact the following more specific structure:

$$\min_{\boldsymbol{x}_g, \boldsymbol{x}_l} \quad \frac{1}{2}\boldsymbol{x}^T\boldsymbol{K}\boldsymbol{x} - \boldsymbol{f}^T\boldsymbol{x} \tag{4.18a}$$

$$\text{s.t.} \quad \boldsymbol{A}\boldsymbol{x}_g = \boldsymbol{b} \tag{4.18b}$$

$$\boldsymbol{x}_l \in \mathcal{K}_l \qquad \text{at each quadrature point} \tag{4.18c}$$

The above problem is then solved with a primal-dual interior point method (IPM) as described in [19, 35], see in particular [17] for more implementation details, and specifically tailored for second-order cone programs. Each iteration of the IPM amounts to solving a Newton system corresponding to the optimality conditions of the above problem. Without going into much details, the specific "local" structure of the problem, in particular the fact that each cone involves local variables which are not coupled by a global operator makes it possible to perform a static condensation for these variables, therefore reducing each Newton iteration to a linear problem of the form:

$$\begin{bmatrix} \boldsymbol{K}_{gg} & \boldsymbol{A}^T \\ \boldsymbol{A} & 0 \end{bmatrix} \begin{Bmatrix} \boldsymbol{x}_g \\ \boldsymbol{\lambda} \end{Bmatrix} = \boldsymbol{r} \tag{4.19}$$

where $\boldsymbol{K}_{gg}$ is similar to a tangent matrix, $\boldsymbol{A}$ is the global constraint matrix (for boundary conditions enforcement for instance), $\boldsymbol{\lambda}$ the associated Lagrange multiplier and the right-hand side $\boldsymbol{r}$ a residual vector. As a result, apart from $\boldsymbol{\lambda}$, each Newton step requires solving a linear problem of size $\Delta\hat{\boldsymbol{u}}$ for the kinematic approach and of size $\hat{\boldsymbol{u}}_e$ for the static approach. The computational cost of one IPM iteration is therefore similar to a standard Newton-Raphson iteration in classical computational elasto-plasticity. IPM classically use direct solvers for solving the linear system. The memory cost is therefore dominated by the Newton system factorization and will also be similar to a standard Newton-Raphson procedure using a direct linear solver. In particular, adding more cones (more plasticity checking points or contact points) do not increase the size of the reduced linear system. However, it has an impact (although quite small in practice compared to Newton-Raphson methods) on the global convergence behaviour of the IPM. As mentioned in [19], the IPM does not require to perform a return mapping on the plasticity surface but instead will enforce the plastic flow rule and yield condition only at the final convergence of the procedure. One attractive aspect is that both equilibrium and behaviour residuals are decreased at the same rate during the procedure. This specific feature makes the solving procedure very robust, especially to large load steps, as it will be illustrated next.

4.4. Dual error estimator and remesh scheme

Finally, following the remeshing strategy considered in [17], we adapt the constitutive error indicator to the case of plasticity, see for instance [47], in addition to the constitutive error induced by surfaces in contact. Using results from both the static and kinematic approaches, the computed error indicator on each element will be used to compute a new mesh-size target map and perform adaptive mesh refinement.

5. Illustrative examples

5.1. Study of a moment-transmitting assembly

This first example aims at illustrating the efficiency of the solving and remesh procedures when applied to a real steel assembly consisting of a particular joint designed for transmitting axial forces and bending moments. This specific joint is not covered by the Eurocodes design rules and must therefore be assessed numerically. Figure 2 gives a general description of the steel assembly and the bolts disposition. It consists of two HEB500 beams of grade S275 ($f_y = 275\,\text{MPa}$) attached to one another using welded 40 mm end-plates of grade S355 ($f_y = 355\,\text{MPa}$) and 20 M27 bolts of grade 8.8 ($f_y = 800\,\text{MPa}$) with no initial stress. The depth of the weld throat is 15 mm thus verifying $2 \times 15 = 30\,\text{mm} \geq t_w = 28\,\text{mm}$ and its yield limit is taken as $f_y = 400\,\text{MPa}$. Steel is modelled as an elastic perfectly plastic material with Young modulus $E = 210\,\text{GPa}$, Poisson ratio $\nu = 0.3$ and yield stress $\sigma_0 = f_y$. Frictionless contact conditions are imposed over the end-plates forbidding penetration. Moreover, the beams are supposed disconnected from the plates so that forces will be transmitted through the welds, thus simulating a small construction gap between the beam ends and the plates.

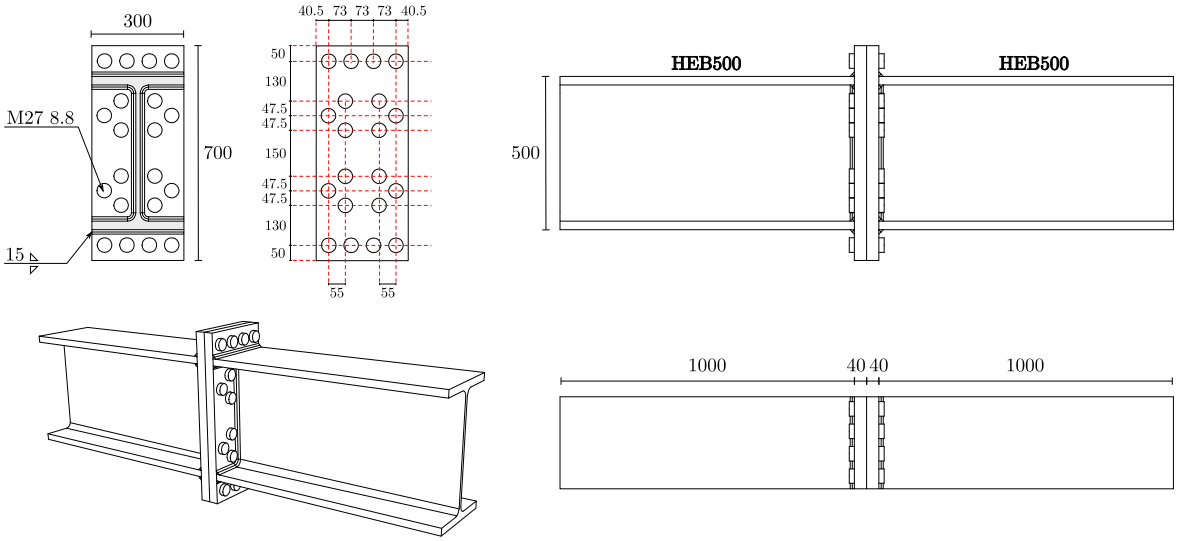

Figure 2: Description of the studied steel assembly

The displacements of all the nodes belonging to the foremost left IPE surface are blocked, and a prescribed displacement composed of a compressive axial displacement (2 mm), a downward vertical displacement (8 mm) and a rotation is imposed (8 mrad), thus simulating an assembly transmitting simultaneously an axial force and a bending moment typically located at mid-span in a structure where shear forces are negligible. Reaction forces are then calculated from the finite element solution.

5.1.1. Convergence analysis

We first perform a convergence analysis of the quantities of interest by solving both kinematic and static approaches in an elasto-plastic setting with a single load-increment step. A 7.5% objective gap between $-J_{\text{stat},h}$ and $J_{\text{kin},h}$ is requested at the beginning of the study and the whole calculation–error maps–remesh scheme is repeated until the desired value is obtained. A total of 4 meshes (one initial mesh and 3 remeshes, see figure 3) were necessary for the gap between the static approach and the kinematic approach with no discontinuities to reach 7.1%, as shown in figure 4. The gap between the static and the kinematic approach with discontinuous elements reaches 3% on the second remesh and an 1.8% on the third remesh. As regards the differences on reaction forces, they followed the same tendency: 9.5% between the static approach and the kinematic approach with no discontinuities and 2.0% between the static and the discontinuous kinematic approach. The different meshes can be seen in figure 3. Figures 5 and 6 show the evolution of the reaction forces in the 4 different meshes.

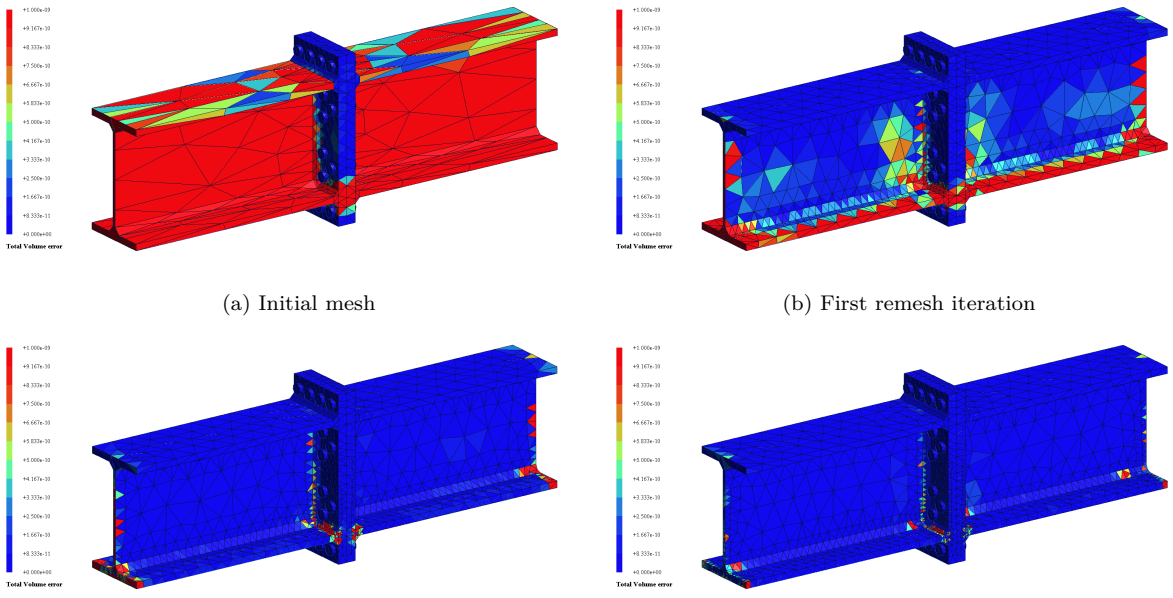

(a) Initial mesh

(b) First remesh iteration

(c) Second remesh iteration

(d) Third remesh iteration

Figure 3: Initial and adapted meshes for the first example, isovalues represent the local computed error

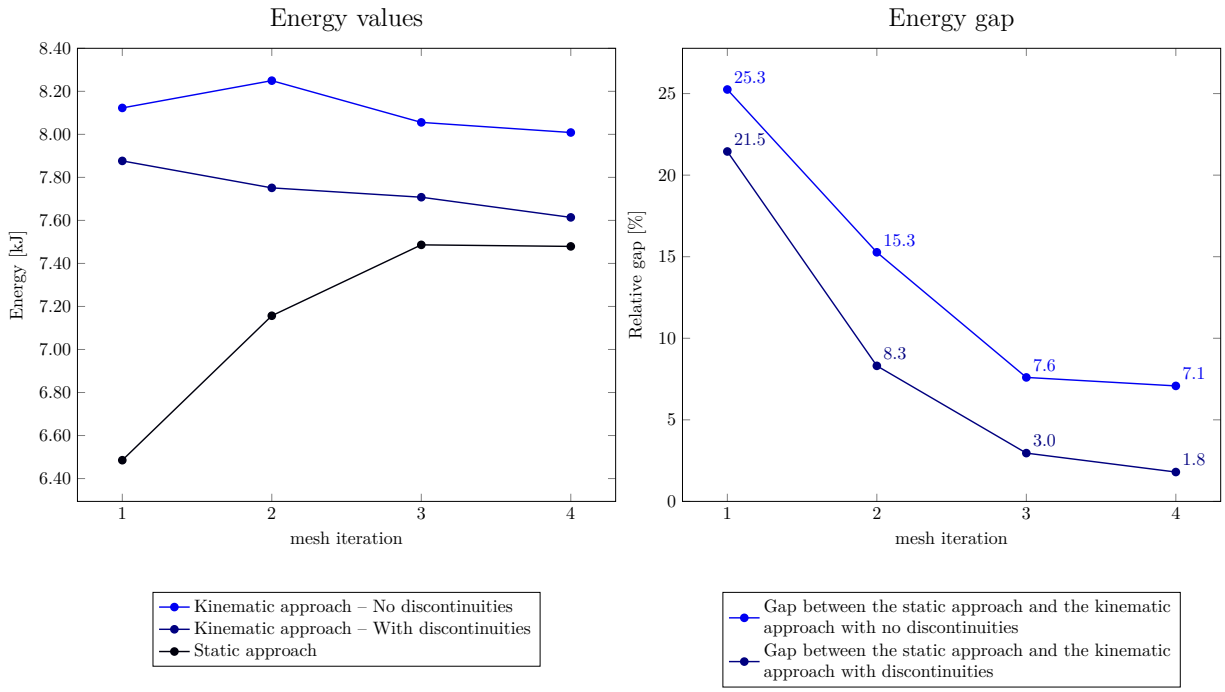

Figure 4: Convergence analysis with respect to objective functions for example 1: $J_{\text{kin},h}$ for the kinematic approach and $-J_{\text{stat},h}$ for the static approach

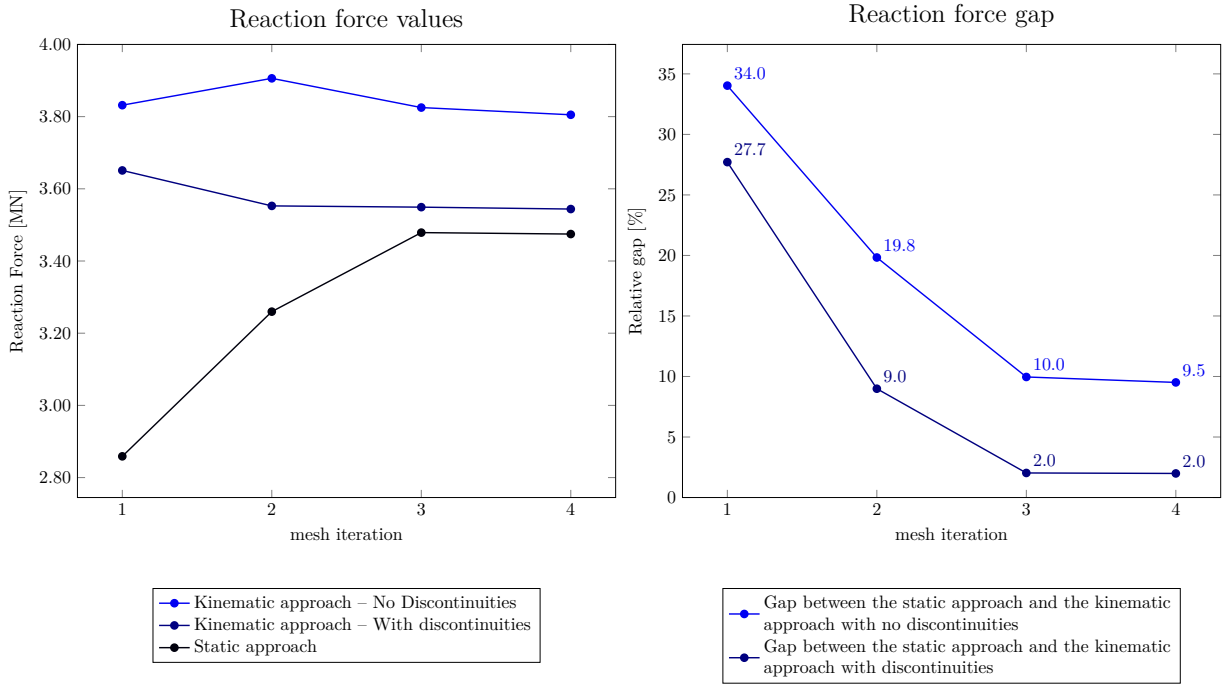

Figure 5: Convergence analysis with respect to the reaction force for example 1

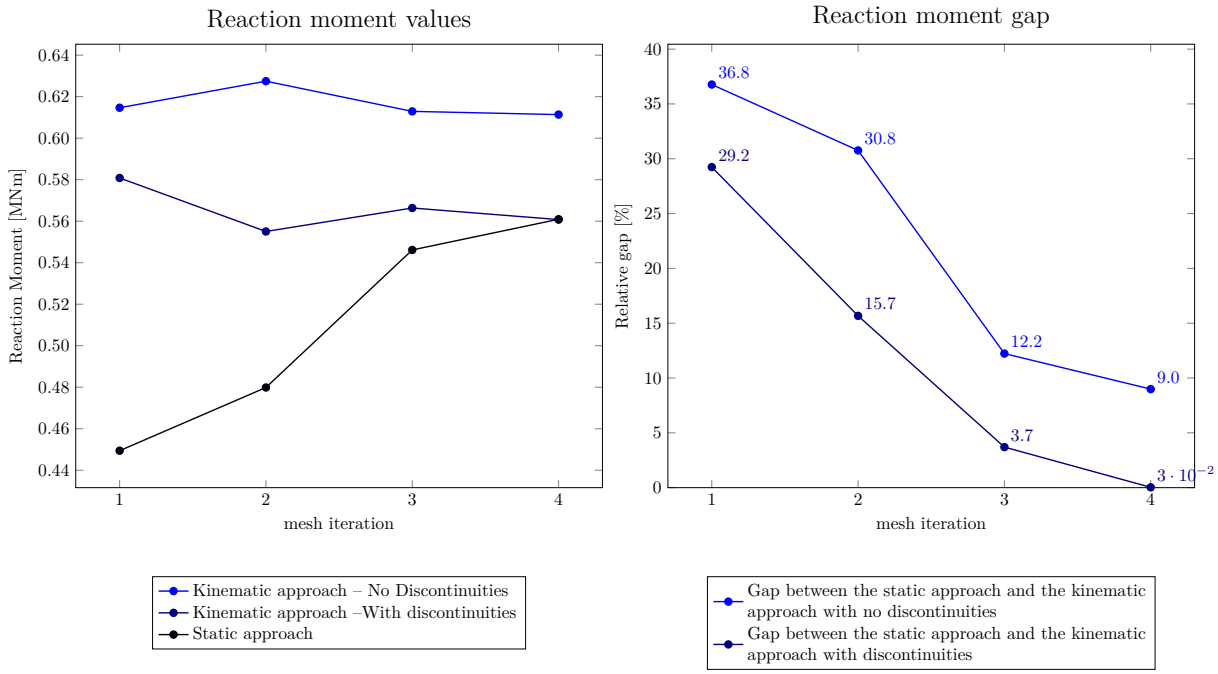

Figure 6: Convergence analysis with respect to the reaction moment for example 1

5.1.2. Determining the interaction diagram

The previous assembly is now compared to a complete HEB500 beam and a hollow beam designed for optimizing material use. Figure 7 describes the hollow beam geometry, typical of those found in practice. The chosen diameter-to-height ratio is taken here equal to 1.45 with a steel grade S275 ($f_y = 275\,\text{MPa}$). As regards the assembly, we consider in fact two different cases:

– Assembly 1: a weaker, badly-designed assembly, where the depth of the weld throat is 10 mm thus being less than the thickness of the flanges;

– Assembly 2: the well-designed assembly introduced before (see figure 2).

In this example, we consider upper and lower bound yield design computations as described in section 3. The reference loading consists of a prescribed bending moment M around the strong axis of the beam and a normal force N. For a fixed value of (N, M), we maximize the load multiplier factor α such that $(\alpha N, \alpha M)$ corresponds to the maximum normal force and bending moment for the chosen reference values. By varying the reference load direction (N, M) in the normal force-bending moment space, we compute different values of the load multiplier α, corresponding to different points on the failure domain, describing, in the end, the beam section interaction diagram. We restrict here the diagram computation to only one quarter, corresponding to tensile force $N \geq 0$ and positive moment $M \geq 0$.

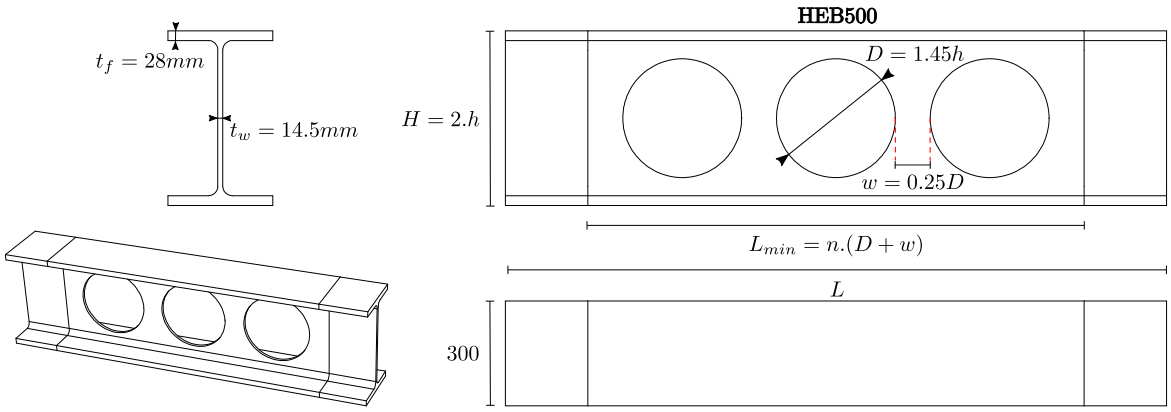

Figure 7: Description of the hollow beam

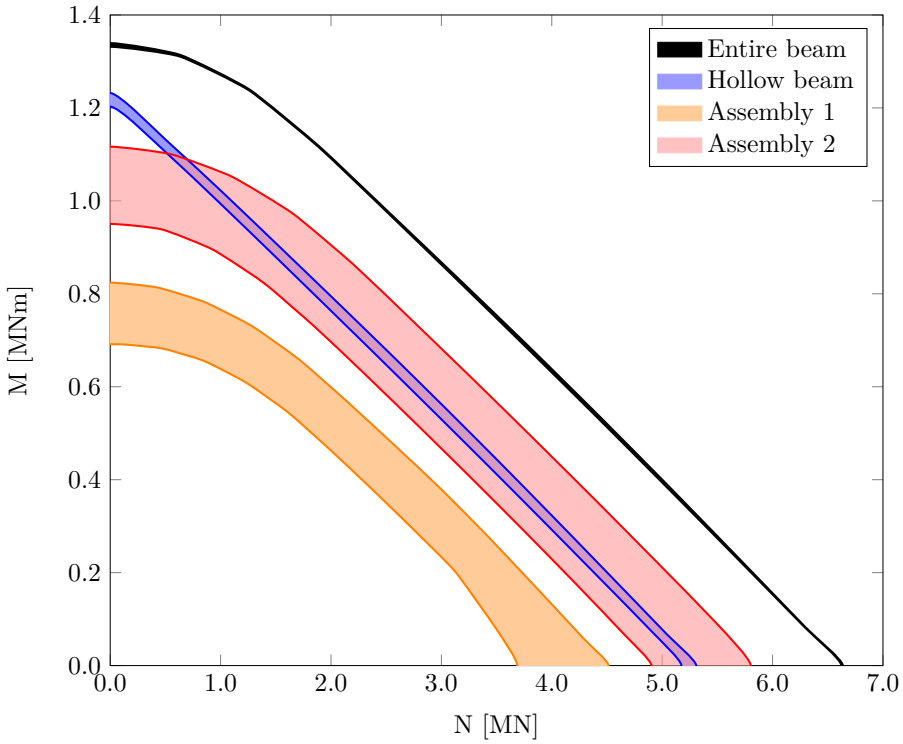

Figure 8: Axial force-bending moment interaction diagram

Figure 8 shows the interaction diagram obtained by following the previous procedure using either upper or lower bound approaches. For each configuration, the corresponding exact interaction diagram boundary lies inside the shaded area delimited by the lower and upper bound calculations. As expected, the hollow beam presents a smaller strength than the entire beam. As regards the assembly, the first topology (assembly 1) with weaker welds exhibits a significantly reduced strength whereas the second one exhibits a strength comparable to that of the hollow beam. In practice, the second assembly presents a better design since the engineer would be able to completely utilize the beam and the assembly strengths. With the first assembly design, the beam would not be fully utilized since failure would be dictated by the weaker assembly. The proposed method provides the engineer the ability to estimate the yielding domain of the studied structure and therefore can be used to give insight on bad conceptions and the possible failure modes which can then be improved. This will ensure a safer and more economical design.

5.2. Performance and result comparison with Abaqus

5.2.1. Convergence analysis

This second example is taken from [17] with some minor changes in boundary conditions. Figure 9 gives the general description of the model. The aim of this example is to assess the proposed procedure computational cost and quality of the obtained results by comparing it with computations made using Abaqus [48]. Abaqus uses classical approaches such as a Newton-Raphson algorithm so solve the global non-linear balance equations along with a return mapping algorithm to correct local plasticity and either a penalty or an augmented Lagragian method to tackle contact conditions. Conversely, our proposed method based on convex optimisation and the interior point algorithm treats all three aspects simultaneously, with plasticity and contact conditions expressed using conic constraints. Aiming at a fair comparison, the same series of 3 iteratively refined meshes is used in all the studies, both for our implementation and for Abaqus computations. Since Abaqus offers continuous displacement-based elements only, the calculation times are compared with respect to our kinematic approach using continuous interpolation. In order to closely compare the numerical performance of both algorithms, all the calculations were made using the same computer (see Table 1). OpenMP technology was used to parallelize over 8 threads.

Figure 9 gives a general description of the model and the three mesh iterations are represented on figure 10. The considered example consists of a HEB200 central column with two IPE360 beams attached over the flanges using welded end-plates and bolts. The end-plates have a 15 mm thickness and 6 M18 bolts are used to connect each beam. We suppose that the bolt hole is equal to its diameter and, to prevent rigid body motions, one of the bolts heads is glued to the plate. For the HEB column, the thickness is 12.7 mm, the same as the IPE flange thickness. The steel grade for all beams and plates is S275 ($f_y = 275\,\text{MPa}$), the bolts are of grade 8.8 ($f_y = 800\,\text{MPa}$) with no initial stress and the yield limit of the welds is taken equal to $f_y = 400\,\text{MPa}$, no hardening being considered here.

Table 1: Computer specifications

Processor	Intel core i7-4700MQ
Number of cores	4
Number of threads	8
Base frequency	2.40 GHz
Maximum frequency	3.40 GHz
Cache	6 MB –SmartCache
RAM	16.0 GB (15.7 GB usable)

A 3 cm vertical displacement is prescribed over the top section of the HEB column and the average displacements of the two end sections of the IPE are blocked.

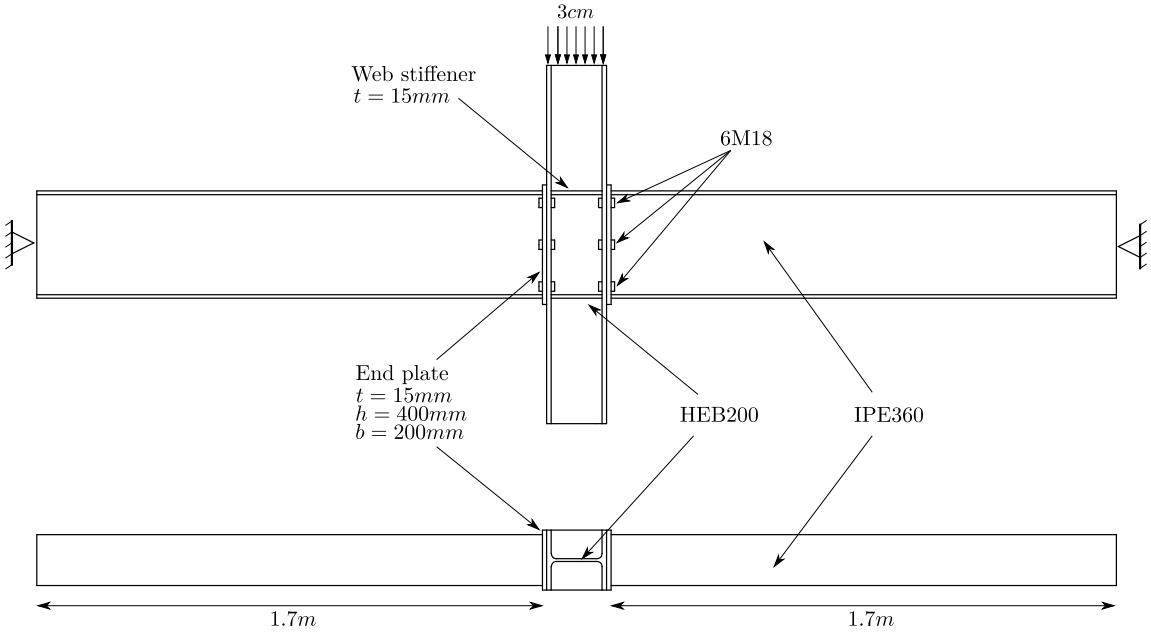

Figure 9: Description of the used model

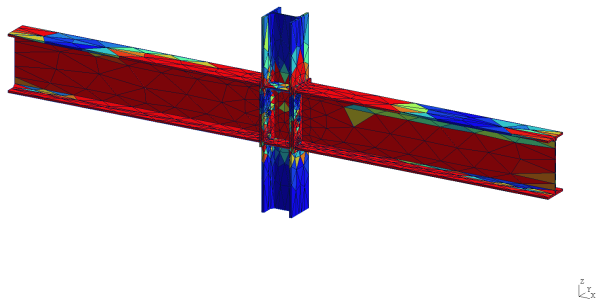

(a) Initial mesh

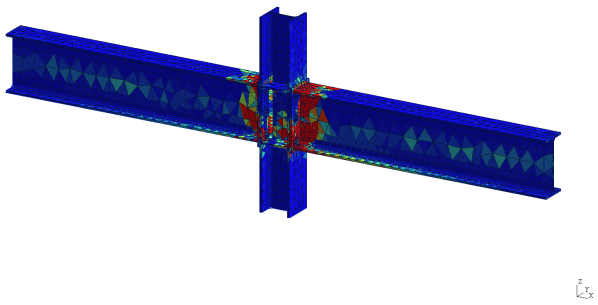

(b) First remesh iteration

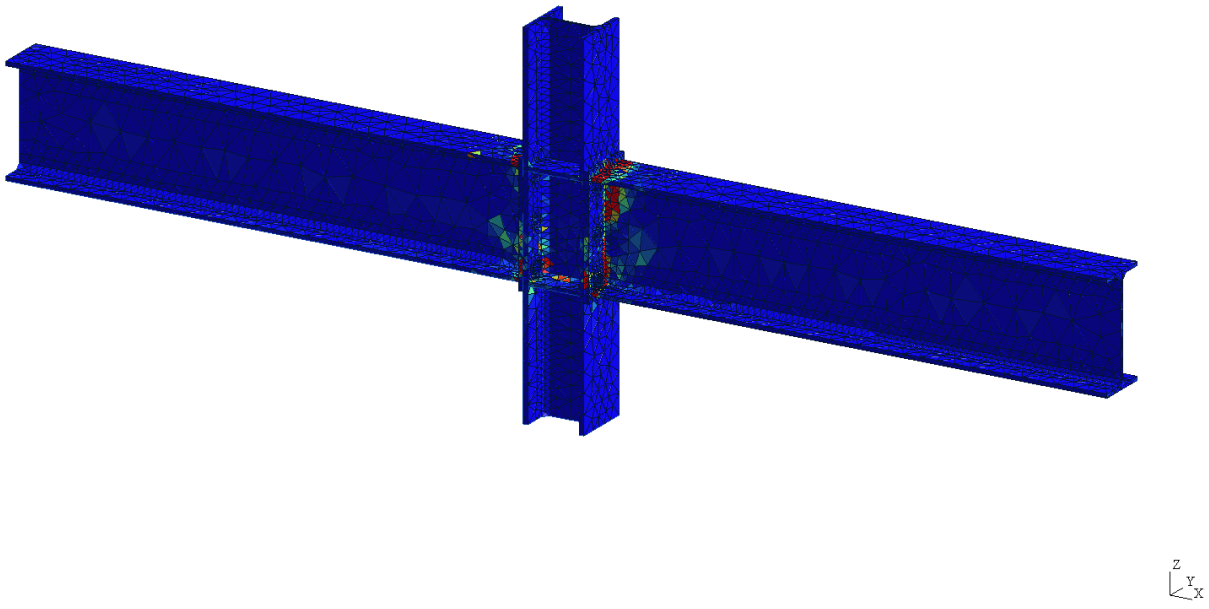

(c) Second remesh iteration

Figure 10: Initial and adapted meshes for the second example, isovalues represent the local computed error

Table 2 shows the CPU times for the different analyses using the 3 different meshes: the kinematic IPM method and Abaqus penalty and augmented Lagrangian methods for treating contact. In this first case, we aim at testing the robustness of the algorithms regarding large load steps. For this purpose, one displacement increment of 3 cm of vertical displacement has been applied to the column. Each solver, using its default options, is given enough time to converge. While with the interior point method, convergence was always ensured with a steady number of iterations $(18 - 21)$, Abaqus could not find a solution in a single load-step and relied on its automatic load incrementation to find a sequence of converged increments until reaching the final prescribed displacement. The number of increments needed depends on the type of approach to solve contact: the penalty approach (PEN) needed 4 to 10 load subdivisions to converge whereas the augmented Lagrangian (AL) required 10 to 13. As a result, although for each increment, the number of iterations to reach convergence is usually smaller than the IPM, in total, the final number of iterations is much higher than the IPM. This obviously has an impact on the total computation cost since one iteration has a similar cost for all methods. One can also note that the IMP method scales well with the system size since the number of iterations only weakly increases. The IPM is largely comparable to Abaqus PEN approach in terms of CPU times with even a small speed-up factor, and compared to the AL approach, a speed-up factor of up to 4.1 can be reached for the last mesh. We therefore obtain similar conclusions in presence of plasticity as those obtained in [17] when considering only contact.

One should note that the dual solution requires as much time to calculate as the primal one since the linear system is roughly the same size. The cost of the error calculation is a simple post-processing step which takes less than 1% of the time needed for the whole resolution which is negligible. As regards the kinematic approach with internal discontinuities, the number of DoF is greater than its continuous counterpart. The solving time is therefore much larger but the results are of better quality. In particular, it is known that volumetric locking appears when dealing with incompressible plasticity. Ten-noded tetrahedra suffer from such a numerical difficulty and hybrid formulations must therefore be used to mitigate the locking effect. On the contrary, discontinuous interpolations are free of any locking problem.

Table 2: CPU times and speed-up factors of the IPM over Abaqus augmented Lagrangian approach and penalty approach for example 2

Remesh iteration	**Mesh Size**	**IPM kinematic approach** (s)$[N_{inc}](N_{iter})$	**Abaqus AL approach** (s)$[N_{inc}](N_{iter})$	**Speed-up factor**	**Abaqus Penalty approach** (s)$[N_{inc}](N_{iter})$	**Speed-up factor**
0	10045	37.5 [1] (18)	137.0 [10] (75)	3.6	45.0 [4] (45)	1.2
1	34017	140.3 [1] (20)	517.0 [13] (93)	3.7	319.0 [9] (55)	2.3
2	63137	243.8 [1] (21)	992.0 [13] (90)	4.1	536.0 [10] (52)	2.2

Global convergence levels with mesh refinement can be assessed using figures 11 and 12. The influence of mesh size over the relative difference between the static and kinematic IP approaches has been represented in figure 11. We can notice that the discontinuous

kinematic approach offers better convergence gaps. A relative difference of nearly less than 10% can be reached with only 2 remesh steps. Regarding the energy values and reaction forces shown in figure 12, we can see that the IPM results coincide with Abaqus AL approach which is known to provide quality results. As for the PEN approach, the values are quite different and that can be explained by some violations of contact constraints as shown in [17].

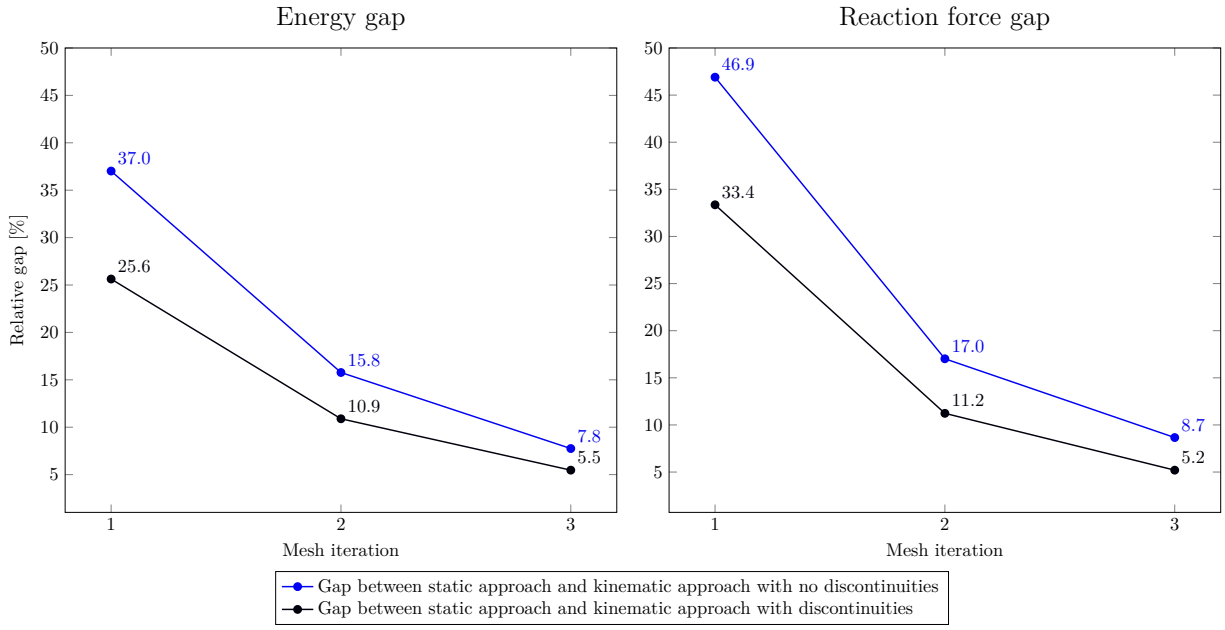

Figure 11: Convergence analysis for example 2

5.2.2. Force to displacements curve

The final mesh obtained from the convergence analysis is used to draw the typical force–displacement curves for the structural system. The prescribed displacement varies from 0 to 3 cm and the total vertical reaction force is then calculated. Figure 13 shows the different curves obtained using the developed approaches and using Abaqus. The adequacy between solutions is clear: Abaqus C3D10I elements provide the same solution as the continuous kinematic approach, the C3D10H hybrid elements provide the same solution as our own implementation of the continuous hybrid approach; all of these solutions are located over the discontinuous kinematic solution which has an upper bound status, itself being larger than the static solution which has a lower bound status.

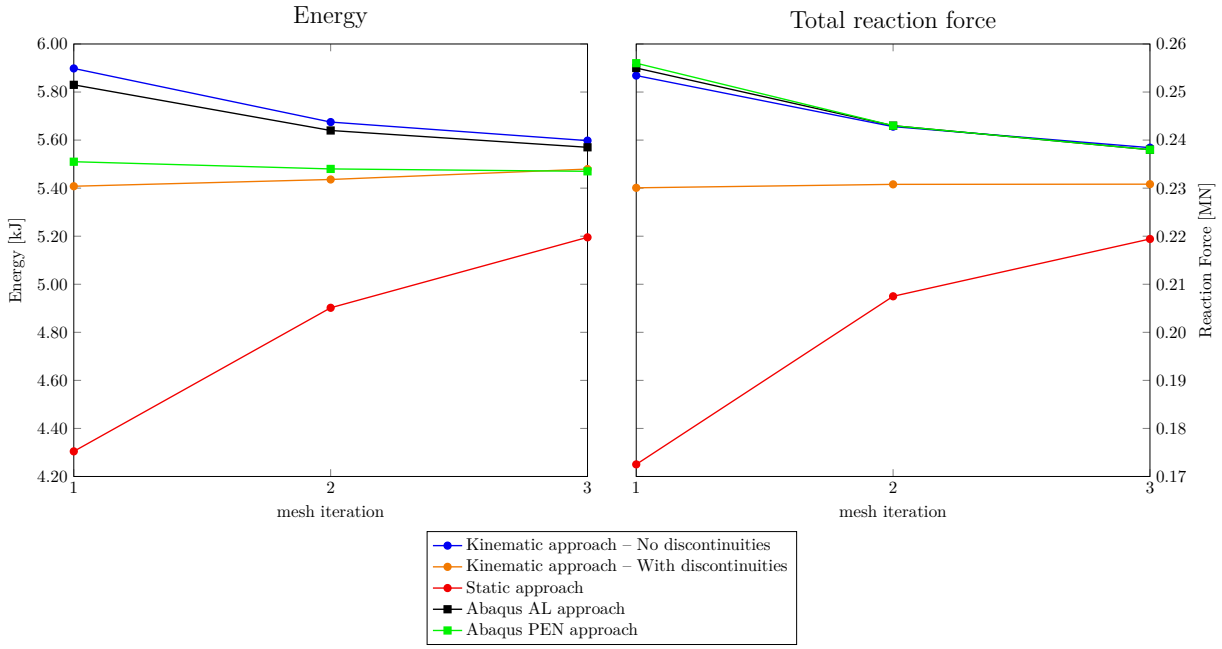

Figure 12: Values comparison with Abaqus

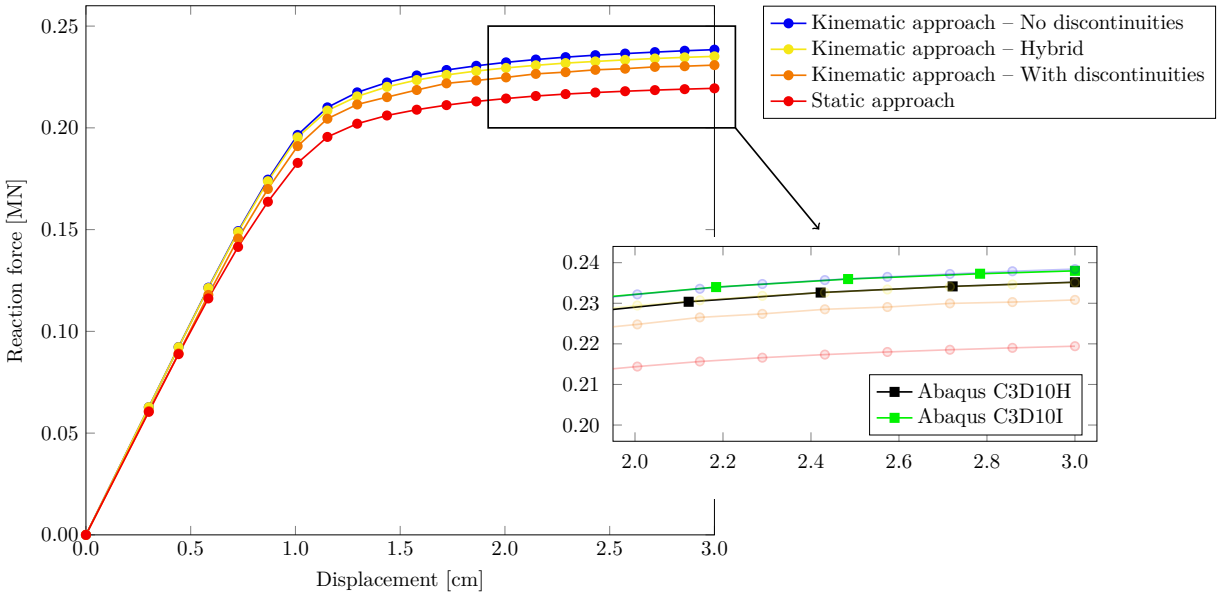

Figure 13: Force–Displacement curves

5.3. Estimation of the ultimate strength of a steel assembly

5.3.1. T-stub resistance

A typical steel-assembly verification according to Eurocode 3 relies on the components method where the complex assembly is divided into basic components. We limit ourselves for more simplicity to the tensile case where the equivalent T-stub method should be used to determine the ultimate resistance. The first step consists in determining the set of components subject to tensile loading under different configurations and subsequently calculating their equivalent T-stub lengths called L_{eff} (see Figure 14). The assembly strength will be obtained as the lowest tensile strength of its different components. In order to validate our proposed yield analysis approach, we compute the strength of a single T-stub and compare it with the semi-analytical formulae proposed by the Eurocode. The description of the various variables in the considered model are represented in figure 15 which is adapted based on Fig. 6.2 of the EN1993-1-8. More precisely, we consider three different variants described in table 3 and, for each of them, the base flange thickness t_f will be varied. The thickness variation will allow us to test the different failure modes proposed by the Eurocode (cf. EN1993-1-8 Table 6.2) and described in figure. 16:

– Mode 1: failure by complete flexural yielding of the flange characterized by the apparition of 4 plastic hinges

$$F_{T,1,Rd} = \frac{4.M_{pl,1,Rd}}{m} \tag{5.1}$$

– Mode 2: failure by partial flexural yielding of the flange characterized by the apparition of 2 plastic hinges, and partial tensile yielding of the bolts

$$F_{T,2,Rd} = \frac{2.M_{pl,2,Rd} + n\sum F_{t,Rd}}{n+m} \tag{5.2}$$

– Mode 3: failure by complete tensile yielding of the bolts

$$F_{T,3,Rd} = \sum_{n_{bolts}} F_{t,Rd} \tag{5.3}$$

– Mode 4: failure by complete tensile yielding of the web

$$F_{T,4,Rd} = L_{eff}.t_w.f_{y,d} \tag{5.4}$$

– Mode 5: failure by complete shear yielding of the welds

$$F_{T,5,Rd} = L_{eff}.(2a_{w,T}).f_{vw,d} \tag{5.5}$$

The detailed description and formulas can be found in Table 6.2 of the EN1993-1-8 and specifically for:

– $M_{pl,1,Rd}$ which is the plastic resisting moment of the flange under failure mode 1;

– $M_{pl,2,Rd}$ which is the plastic resisting moment of the flange under failure mode 2;

– $n = \min(e,\ 1.25m)$ which is a geometrical parameter that depends of the position of the bolts.

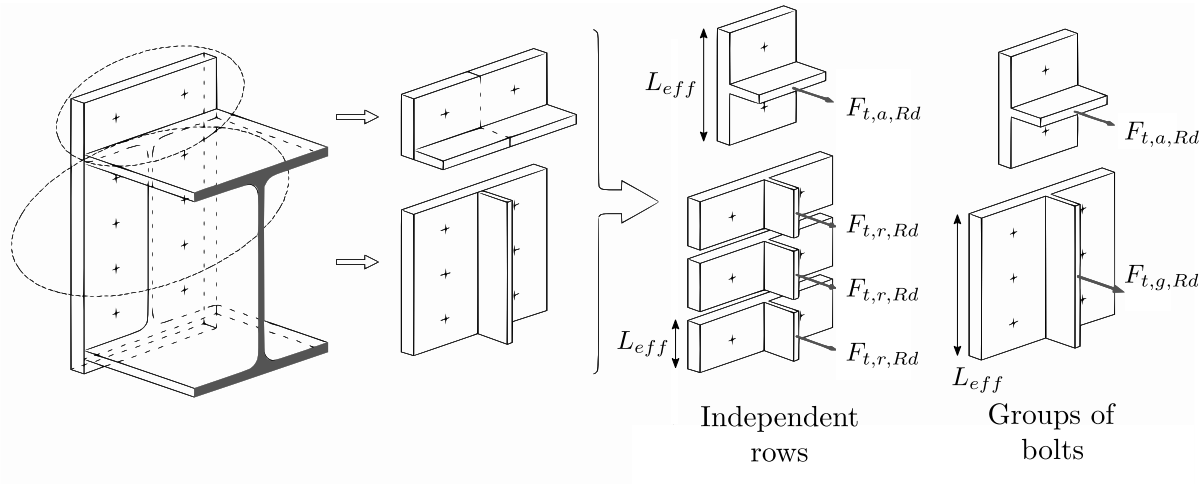

Figure 14: A descriptive explanation of the components method

Stiff bolts are used in model 1, therefore no yielding is expected in the bolts. Since $2a \leq t_w$, we expect that the welds will yield before the web since their yield strength under shear loading is less than the one for the web under tensile loading. We then expect a failure of type 1 for thin flanges and of type 5 for thick flanges. In models 2 and 3, smaller bolts are used, therefore modes 2 and 3 are expected to appear depending of the thickness of the flanges. In model 3, we chose $2a > t_w$ so that the yielding will occur in the web.

Table 3: Descriptions

Model name	**Length** L (mm)	**Web**			**Flange**			**Welds**		**Bolts**			**Expected failure modes**
		t_w (mm)	h_w (mm)	f_{uw} (MPa)	t_f (mm)	b_f (mm)	f_{uf} (MPa)	a (mm)	f_{vw} (MPa)	Type	f_{ub} (MPa)	e (mm)	
Model 1	100	10	100	355	Variable	300	355	5	205	M20-10.9	1000	50	1 – 5
Model 2	100	10	100	355	Variable	300	355	5	205	M14-10.9	1000	50	1 – 2 – 5
Model 3	100	11	100	355	Variable	300	355	8	205	M14-10.9	1000	50	1 – 2 – 3

The obtained results are presented in figure 17. Using the upper and lower bound yield analysis, we obtain a very satisfying estimate of the T-stub strength as proposed by the Eurocode. The obtained failure mechanisms are in accordance with the expected modes. For example, figure 18 illustrates the three different failure modes obtained with the third model when varying the flange thickness: complete flexural yielding of the flange (Mode 1) for a thin flange ($t_f = 10\,\text{mm}$), partial flexural yielding of the flange and tensile yielding

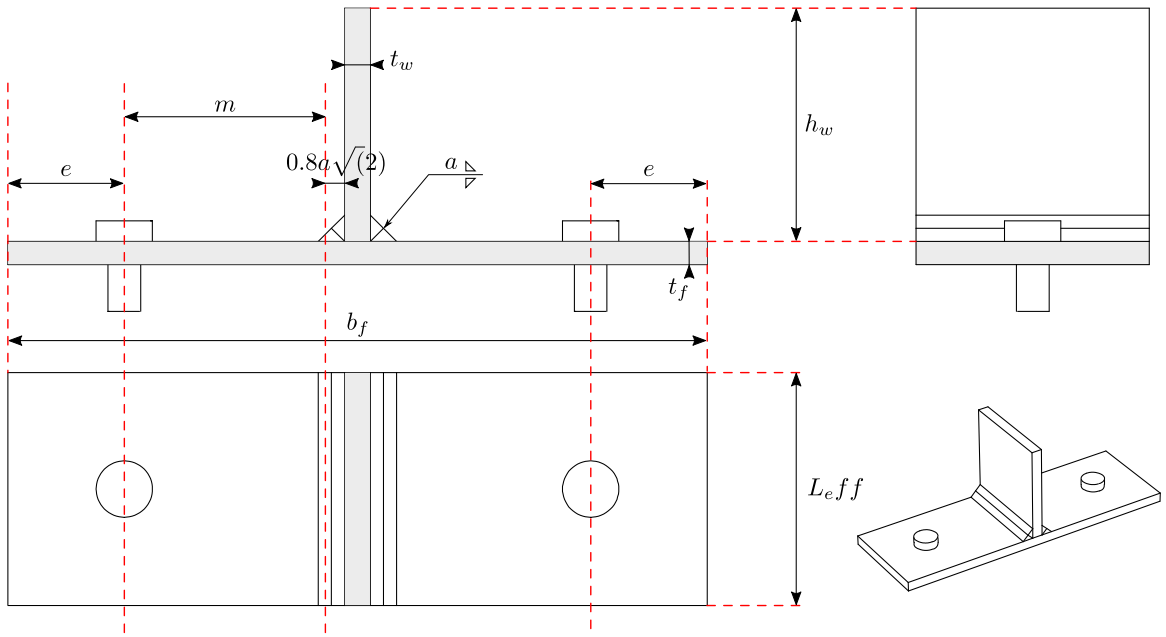

Figure 15: Description of the used model

of the bolts (Mode 2) for a moderately thick flange ($t_f = 25\,\text{mm}$) and a complete yielding of the bolts (Mode 3) with a thick flange ($t_f = 40\,\text{mm}$). The small differences observed in figure 17 with respect to the Eurocode semi-analytical formulae are due to the fact that the latter are obtained from 2D failure modes while our model is fully 3D. For instance, yield lines of modes 1 and 2 are considered straight of length L_{eff}, while our computations produce curved yield lines depending on the depth of the analysed model.

5.3.2. Resistance of a base column under tensile loading

The proposed approach can be generalized to more complex assemblies, such as a classical base column under tensile loading as shown in figure 19. The HEB column is welded to a base plate which is bolted to its final support. In order to determine the resistance of this assembly, more than 20 sub-components should be analysed. For each of them, all failure modes of the corresponding equivalent T-stub should be checked. The yield design approach can provide valuable insight on the failure mode and the shape of the yield lines as seen in figure 21, therefore reducing considerably the computational effort required to verify this assembly. A complete Eurocode check identifies the yield line mechanism of figure 20 as the most critical one. The manual computation of this simplified mechanism gives a yield strength of $F_{T,rd} = 312\,\text{kN}$ while the proposed approaches give $F_{T,upper} = 354\,\text{kN}$ using the upper bound approach and $F_{T,lower} = 335\,\text{kN}$ using the lower bound approach. The small difference is again due to the fact that the Eurocode does not take into consideration 3D effects nor the complete curvature seen in the yield line nor the contribution of the bolt heads to the assembly strength. The resistance value given by the

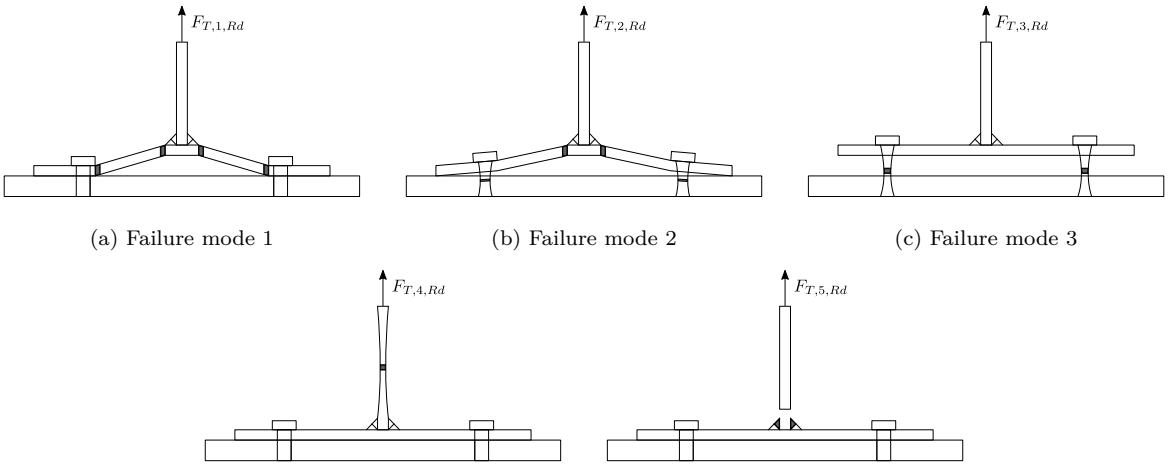

(a) Failure mode 1 (b) Failure mode 2 (c) Failure mode 3

(d) Failure mode 4 (e) Failure mode 5

Figure 16: Different failure modes proposed by the Eurocode

Eurocode is therefore slightly more conservative.

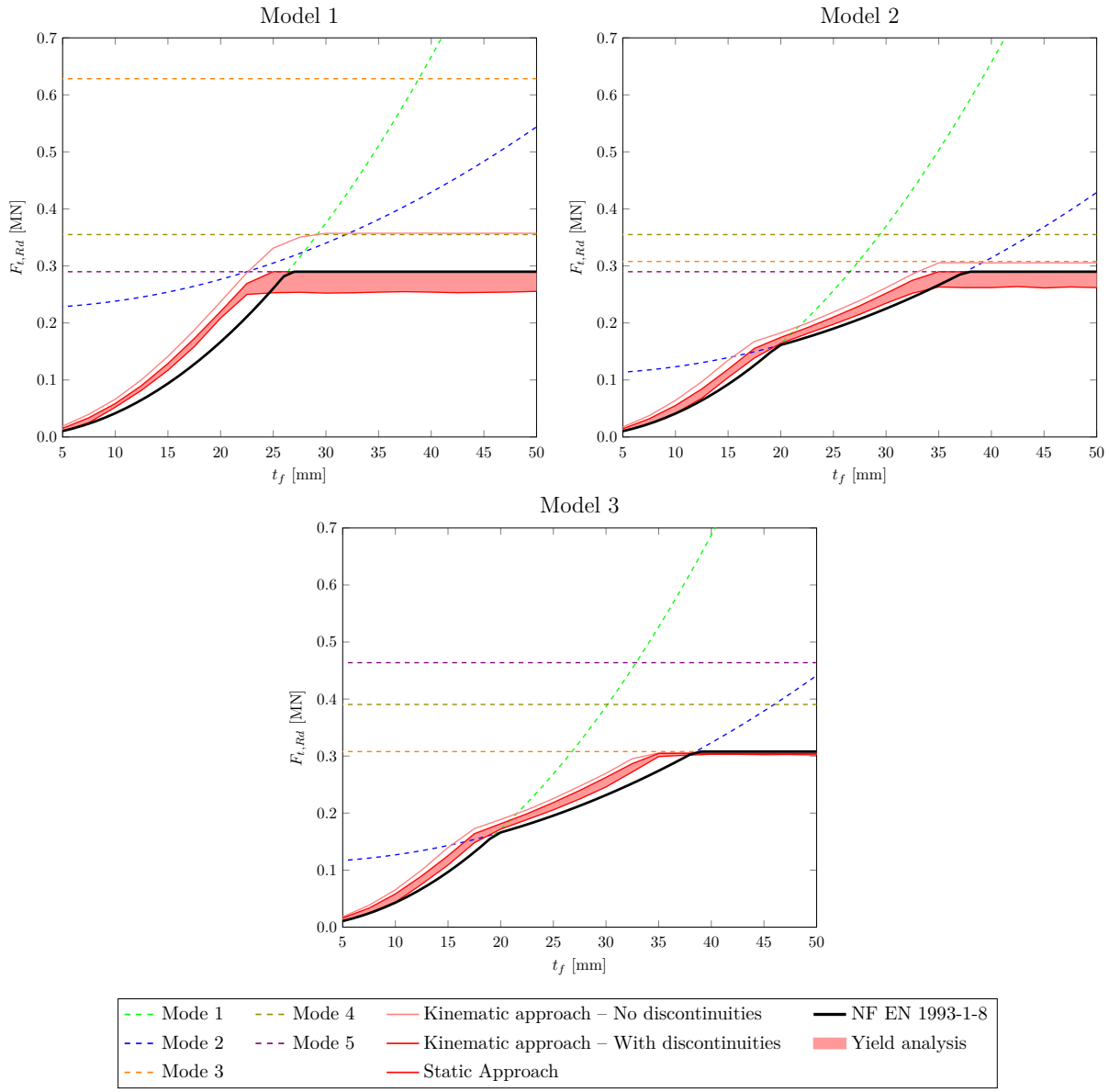

Figure 17: Results comparisons with the Eurocode (NF EN 1993-1-8)

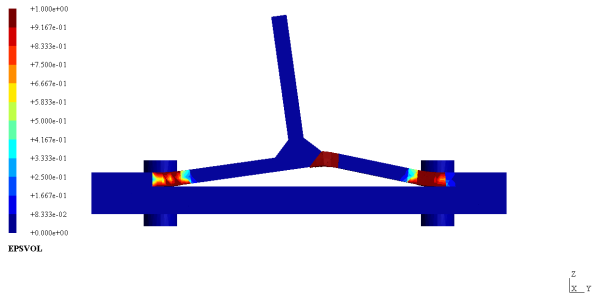

(a) Model 3 – $t_f = 10\,\text{mm}$ – Failure mode 1

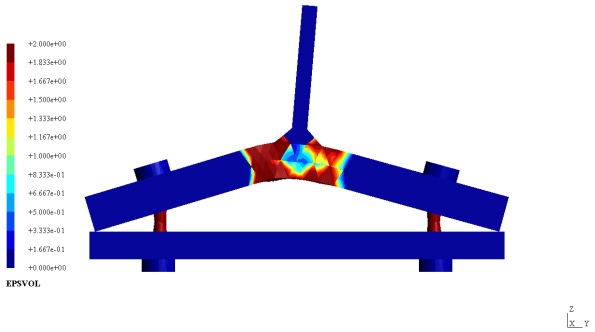

(b) Model 3 – $t_f = 25\,\text{mm}$ – Failure mode 2

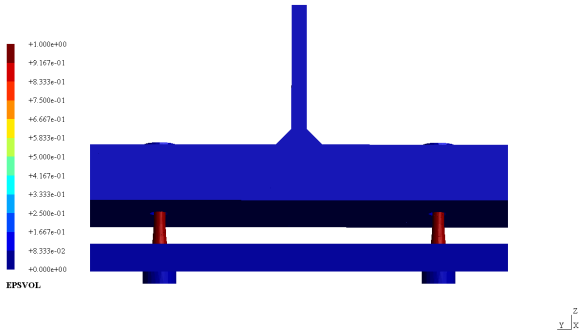

(c) Model 3 – $t_f = 40\,\text{mm}$ – Failure mode 3

Figure 18: Different failure modes obtained for 3 configurations of the third model (colours correspond to the plastic dissipation)

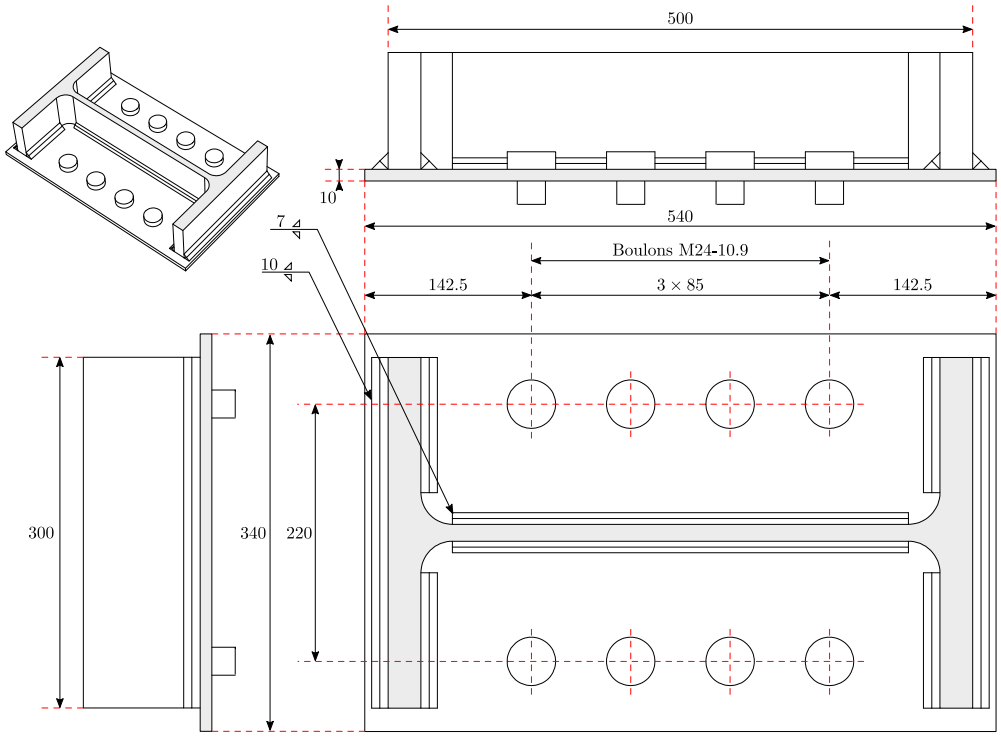

Figure 19: Description of the used model

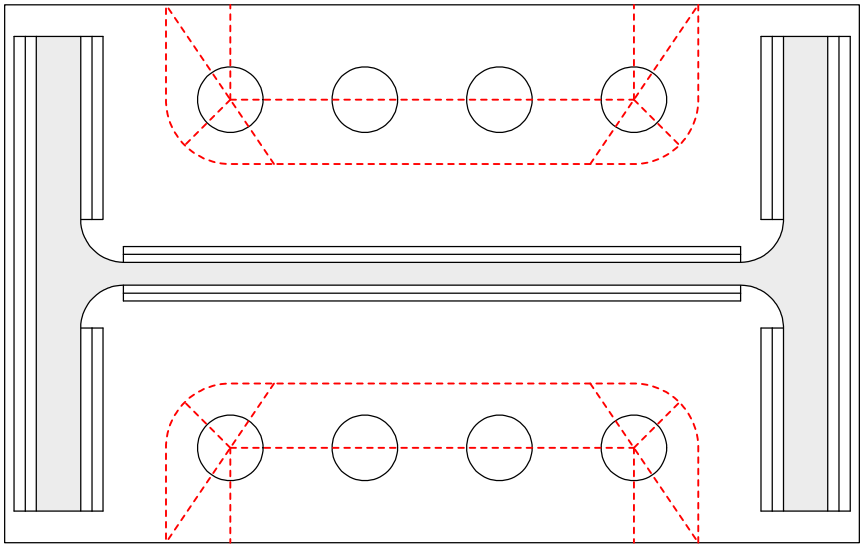

Figure 20: Expected yield mechanism (the dashed red lines represent yield lines)

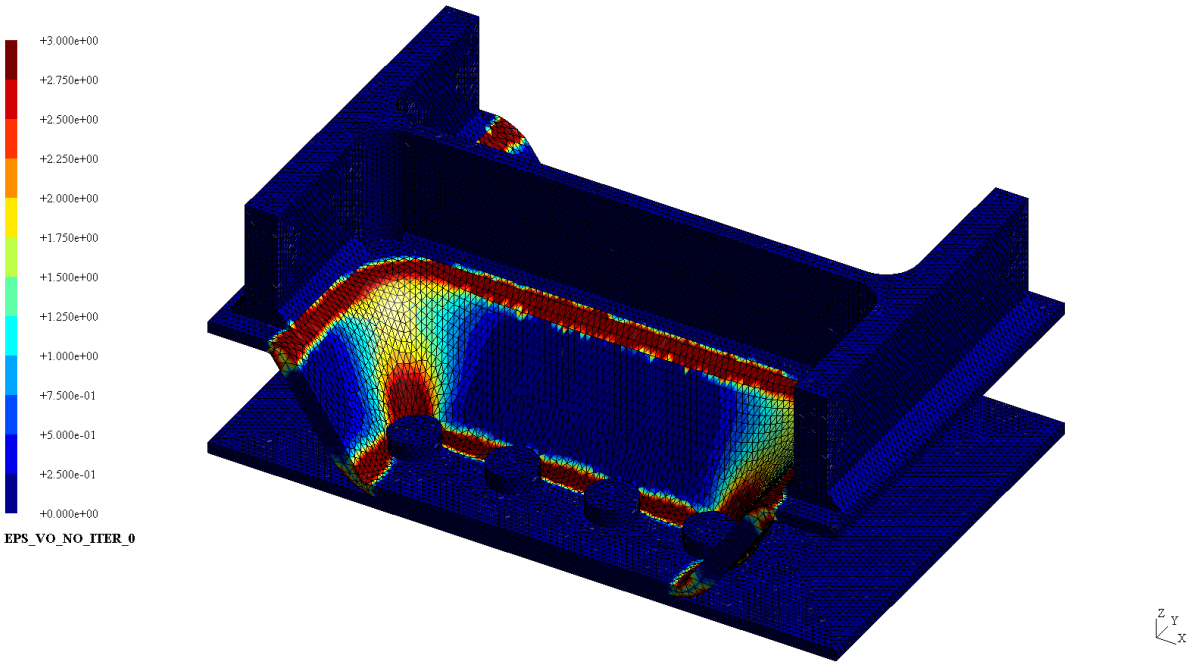

(a) Failure mode obtained by the upper bound yield analysis

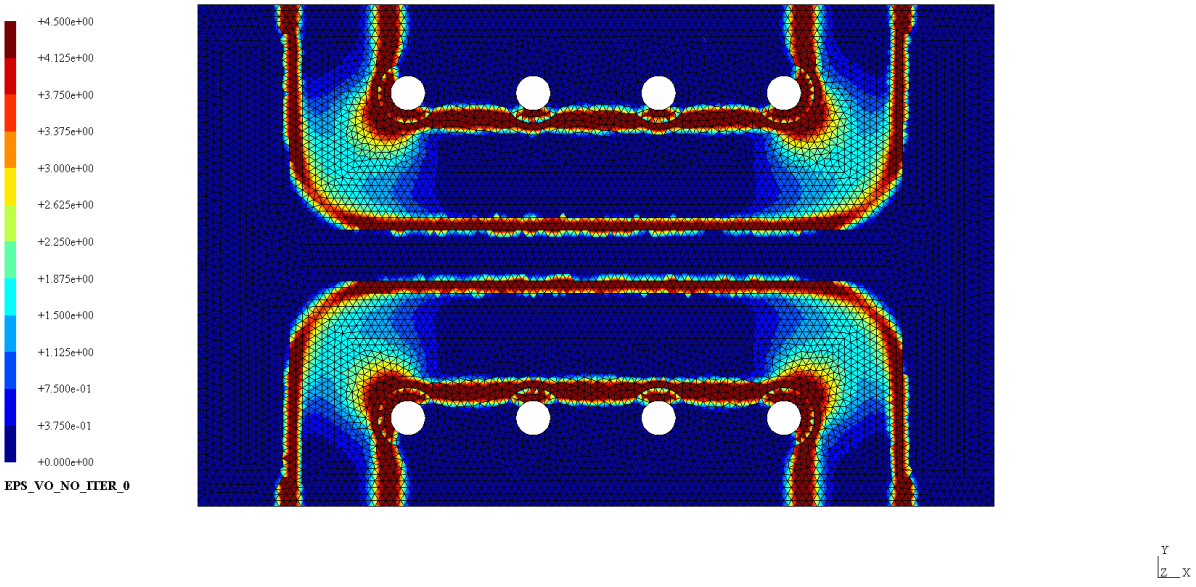

(b) Plastic dissipation concentration matches the expected shape of the yield lines in figure 20

Figure 21: Solution of the upper bound yield analysis approach

6. Conclusions and perspectives

Modelling three-dimensional elasto-plastic steel structures (including also contact) using SOCP and IPM has been investigated in this paper. Two kinematic and static variational principles are considered, leading to the formulation of convex minimization problems. Computation of the structure ultimate load using limit analysis concepts can be obtained as a particular case of the elasto-plastic variational problems with only minor modifications. Besides, assuming a radial loading path, limit loads can also be computed from the elasto-plastic problems using a single large load step, without the need to perform a step-by-step load subdivision. Robustness of the solution procedure to large load steps is ensured by resorting to a primal-dual interior point method which is really efficient for SOCP problems.

The use of a dual analysis based on both a kinematic and static approach enables to assess the solution convergence by comparing their associated energies. The comparison of local fields also enables to compute an error indicator used for adaptive remeshing. The static-based solution has also the interesting property of being a lower-bound to the true solution. It is, therefore, a safer solution in terms of stress quantities than a displacement-based solution, which is appealing in the context of safety verification including elasto-plastic behaviour and limit load computations.

The robustness and efficiency of the solution procedure has been compared against Abaqus elasto-plastic computations. When aiming at computing a fully yielded solution, the computational benefit of performing only one large load step compared to a standard step-by-step Newton procedure is quite important. Limit load computations can therefore be obtained at reasonable computational cost and offer a very useful design aid for the engineer as shown by the considered example. In particular, we have demonstrated that our numerical tool enables to retrieve the different failure modes of a T-stub considered by the Eurocodes, both qualitatively and quantitatively but also offers a very useful way to analyse a complex assembly without having to consider all potential individual failure modes of its different components.

Further developments may include a more realistic description of the frictional behaviour as indicated in [17] or an improvement of the computational cost of the IPM for large 3D problems by resorting to iterative solver for solving the different Newton steps. Devising efficient warm-start strategies such as [15, 22], currently not exploited by our IPM implementation, would be a valuable improvement to the overall procedure efficiency. Another interesting line of development would be to investigate how geometrically non-linear effects could be included in the proposed numerical analysis.

References

[1] R. Hill, The mathematical theory of plasticity, Clarendon Press, Oxford, 1950.

[2] J. Salençon, Calcul à la rupture et analyse limite, Presses de l'Ecole Nationale des Ponts et Chaussées, 1983.

[3] J. Salençon, Yield Design, London, Hoboken : ISTE Ltd., John Wiley & Sons, Inc., 2013.

[4] W.-F. Chen, Limit analysis and soil plasticity, Elsevier, 2013.

[5] J. Schlaich, K. Schäfer, M. Jennewein, Toward a consistent design of structural concrete, PCI journal 32 (3) (1987) 74–150.

[6] K. Johansen, Yield-line theory, Cement and Concrete Association London, 1962.

[7] M. Save, Atlas of limit loads of metal plates, shells and disks, North-Holland Series in Applied Mathematics & Mechanics, Elsevier Science Ltd, 1995.

[8] M. A. Save, C. E. Massonnet, G. de Saxce, Plastic limit analysis of plates, shells, and disks, North Holland, 1997.

[9] A. Makrodimopoulos, C. M. Martin, Lower bound limit analysis of cohesive-frictional materials using second-order cone programming, International Journal for Numerical Methods in Engineering 66 (4) (2006) 604–634. doi:10.1002/nme.1567.
URL http://doi.wiley.com/10.1002/nme.1567

[10] A. Makrodimopoulos, C. M. Martin, Upper bound limit analysis using simplex strain elements and second-order cone programming, International Journal for Numerical and Analytical Methods in Geomechanics 31 (6) (2007) 835–865. doi:10.1002/nag.567.
URL http://doi.wiley.com/10.1002/nag.567

[11] C. M. Martin, A. Makrodimopoulos, Finite-element limit analysis of Mohr–Coulomb materials in 3d using semidefinite programming, Journal of engineering mechanics 134 (4) (2008) 339–347.

[12] H. Vincent, M. Arquier, J. Bleyer, P. de Buhan, Yield design-based numerical analysis of three-dimensional reinforced concrete structures, International Journal for Numerical and Analytical Methods in Geomechanics 42 (18) (2018) 2177–2192.

[13] K. Krabbenhoft, A. Lyamin, J. Huang, M. V. da Silva, Granular contact dynamics using mathematical programming methods, Computers and Geotechnics 43 (2012) 165–176.

[14] X. Zhang, K. Krabbenhoft, D. Sheng, Particle finite element analysis of the granular column collapse problem, Granular Matter 16 (4) (2014) 609–619.

[15] Y. Kanno, Nonsmooth mechanics and convex optimization, CRC Press, Boca Raton, FL, 2011.

[16] Y. Kanno, J. A. C. Martins, A. Pinto da Costa, Three-dimensional quasi-static frictional contact by using second-order cone linear complementarity problem, International Journal for Numerical Methods in Engineering 65 (1) (2006) 62–83. doi:10.1002/nme.1493.

[17] C. El Boustani, J. Bleyer, M. Arquier, M.-K. Ferradi, K. Sab, Dual finite-element analysis using second-order cone programming for structures including contact, Engineering Structures.

[18] J. Bleyer, M. Maillard, P. De Buhan, P. Coussot, Efficient numerical computations of yield stress fluid flows using second-order cone programming, Computer Methods in Applied Mechanics and Engineering 283 (2015) 599–614.

[19] J. Bleyer, Advances in the simulation of viscoplastic fluid flows using interior-point methods, Computer Methods in Applied Mechanics and Engineering 330 (2018) 368–394.

[20] K. Krabbenhoft, A. V. Lyamin, S. W. Sloan, P. Wriggers, An interior-point algorithm for elastoplasticity, International Journal for Numerical Methods in Engineering 69 (3) (2007) 592–626. doi:10.1002/nme.1771.
URL http://doi.wiley.com/10.1002/nme.1771

[21] K. Krabbenhøft, A. Lyamin, S. Sloan, Formulation and solution of some plasticity problems as conic programs, International Journal of Solids and Structures 44 (5) (2007) 1533–1549. doi:10.1016/j.ijsolstr.2006.06.036.
URL http://linkinghub.elsevier.com/retrieve/pii/S0020768306002447

[22] K. Yonekura, Y. Kanno, Second-order cone programming with warm start for elastoplastic analysis with von Mises yield criterion, Optimization and Engineering 13 (2) (2012) 181–218. doi:10.1007/s11081-011-9144-4.
URL https://link.springer.com/article/10.1007/s11081-011-9144-4

[23] G. Maier, A quadratic programming approach for certain classes of non linear structural problems, Meccanica 3 (2) (1968) 121–130. doi:10.1007/BF02129011.
URL http://link.springer.com/10.1007/BF02129011

[24] G. Maier, Complementary plastic work theorems in piecewise-linear elastoplasticity, International Journal of Solids and Structures 5 (3) (1969) 261–270. doi:10.1016/0020-7683(69)90063-8.
URL https://linkinghub.elsevier.com/retrieve/pii/0020768369900638

[25] M. Capurso, G. Maier, Incremental elastoplastic analysis and quadratic optimization, Meccanica 5 (2) (1970) 107–116. doi:10.1007/BF02134214.
URL http://link.springer.com/10.1007/BF02134214

[26] P. W. Christensen, A nonsmooth newton method for elastoplastic problems, Computer Methods in Applied Mechanics and Engineering 191 (11-12) (2002) 1189–1219.

[27] O. Sander, P. Jaap, Solving primal plasticity increment problems in the time of a single predictor–corrector iteration, Computational Mechanics (2019) 1–23.

[28] A. Bilotta, L. Leonetti, G. Garcea, An algorithm for incremental elastoplastic analysis using equality constrained sequential quadratic programming, Computers & structures 102 (2012) 97–107.

[29] Y. Kanno, A fast first-order optimization approach to elastoplastic analysis of skeletal structures, Optimization and Engineering 17 (4) (2016) 861–896.

[30] G. De Saxcé, Z. Q. Feng, The bipotential method: A constructive approach to design the complete contact law with friction and improved numerical algorithms, Mathematical and Computer Modelling 28 (4) (1998) 225–245. doi:10.1016/S0895-7177(98)00119-8.
URL http://www.sciencedirect.com/science/article/pii/S0895717798001198

[31] M. Hjiaj, J. Fortin, G. de Saxcé, A complete stress update algorithm for the non-associated Drucker–Prager model including treatment of the apex, International Journal of Engineering Science 41 (10) (2003) 1109–1143. doi:10.1016/S0020-7225(02)00376-2.
URL https://linkinghub.elsevier.com/retrieve/pii/S0020722502003762

[32] A. Makrodimopoulos, Remarks on some properties of conic yield restrictions in limit analysis, International Journal for Numerical Methods in Biomedical Engineering 26 (11) (2010) 1449–1461.

[33] M. S. Lobo, L. Vandenberghe, S. Boyd, H. Lebret, Applications of second-order cone programming, Linear Algebra and its Applications 284 (1-3) (1998) 193–228. doi:10.1016/S0024-3795(98)10032-0.
URL http://linkinghub.elsevier.com/retrieve/pii/S0024379598100320

[34] S. P. Boyd, L. Vandenberghe, Convex optimization, Cambridge University Press, Cambridge, UK ; New York, 2004.

[35] E. Andersen, C. Roos, T. Terlaky, On implementing a primal-dual interior-point method for conic quadratic optimization, Mathematical Programming 95 (2) (2003) 249–277. doi:10.1007/s10107-002-0349-3.
URL http://link.springer.com/10.1007/s10107-002-0349-3

[36] M. Wright, The interior-point revolution in optimization: history, recent developments, and lasting consequences, Bulletin of the American mathematical society 42 (1) (2005) 39–56.

[37] M. Ortiz, L. Stainier, The variational formulation of viscoplastic constitutive updates, Computer Methods in Applied Mechanics and Engineering 171 (3-4) (1999) 419–444. doi:10.1016/S0045-7825(98)00219-9.
URL https://linkinghub.elsevier.com/retrieve/pii/S0045782598002199

[38] C. Miehe, Strain-driven homogenization of inelastic microstructures and composites based on an incremental variational formulation, International Journal for numerical methods in engineering 55 (11) (2002) 1285–1322.

[39] A. V. Lyamin, S. W. Sloan, Lower bound limit analysis using non-linear programming, International Journal for Numerical Methods in Engineering 55 (5) (2002) 573–611.

[40] A. V. Lyamin, S. W. Sloan, Upper bound limit analysis using linear finite elements and non-linear programming, International Journal for Numerical and Analytical Methods in Geomechanics 26 (2) (2002) 181–216.

[41] J. P. M. de Almeida, E. A. Maunder, Equilibrium Finite Element Formulations, John Wiley & Sons, Ltd, Chichester, UK, 2017. doi:10.1002/9781118925782.
URL http://doi.wiley.com/10.1002/9781118925782

[42] M. Kempeneers, J.-F. Debongnie, P. Beckers, Pure equilibrium tetrahedral finite elements for global error estimation by dual analysis, International Journal for Numerical Methods in Engineering (2009) n/a–n/adoi:10.1002/nme.2703.
URL http://doi.wiley.com/10.1002/nme.2703

[43] T. H. H. PIAN, Derivation of element stiffness matrices by assumed stress distributions, AIAA Journal 2 (7) (1964) 1333–1336. doi:10.2514/3.2546.
URL https://doi.org/10.2514/3.2546

[44] G. Morera, Soluzione generale delle equazioni indefinite dell'equilibrio di un corpo continuo, Atti Accad. Naz. Lincei, Rend. Cl. Fis. Mat. Natur., V. Ser 1 (1) (1892) 137–141.

[45] J. C. Maxwell, On reciprocal diagrams in space, and their relation to Airy's function of stress, Proceedings of the London Mathematical Society 1 (1) (1866) 58–63.

[46] J. P. M. De Almeida, O. J. B. A. Pereira, A set of hybrid equilibrium finite elements models for the analysis of three dimensional solids, International Journal for Numerical Methods in Engineering 39 (16) (1996) 2789–2802. doi:10.1002/(SICI)1097-0207(19960830)39:16<2789::AID-NME976>3.0.CO;2-J.
URL http://doi.wiley.com/10.1002/%28SICI%291097-0207%2819960830%2939%3A16%3C2789%3A%3AAID-NME976%3E3.0.CO%3B2-J

[47] P. Ladevèze, J. P. Pelle, Mastering calculations in linear and nonlinear mechanics, Mechanical engineering series, Springer Science, New York, 2005.

[48] M. Smith, ABAQUS/Standard User's Manual, Version 6.9, Simulia, 2009.